

Laminar boundary layer forcing with active surface deformations

Bradley Gibeau and Sina Ghaemi^{✉*}*Department of Mechanical Engineering, University of Alberta, Edmonton, T6G 2R3, Canada*

(Received 29 June 2022; accepted 13 October 2022; published 2 November 2022)

We experimentally evaluate the use of active wall-normal surface deformations as a method of actuation for the control of wall-bounded flows. Circular surface deformations are generated locally beneath a laminar boundary layer at a Reynolds number of $Re_{\delta^*} = 340$, where δ^* is the displacement thickness, and high-speed particle image velocimetry is used to investigate how the resulting motions vary as a function of the frequency and amplitude of actuation. We consider frequencies ranging from $St = 0.1$ to 1.0 where St is the Strouhal number based on the actuator diameter and freestream velocity, and amplitudes ranging from 0.005 to 0.020 times the actuator diameter (0.12 to 0.49 times the local boundary-layer thickness). We find that the actuation strategy can effectively produce both high- and low-speed motions with similar magnitudes which reach up to roughly one-third of the freestream velocity in some cases. The frequency of actuation dictates the spatial structure of these motions, while the amplitude of actuation dictates their strength. The motions are found to vary considerably, with $St = 0.1, 0.2, 0.6,$ and 0.7 producing single flow structures concentrated along the centerline of the actuator (type-1 modes) while the remaining St produce structures with double extrema displaced in the spanwise directions (type-2 modes). Overall, the results indicate that surface deformations at the lowest frequencies ($St \leq 0.2$) are the most promising for flow control because the resulting motions are stronger, more stable, and are concentrated along the centerline of the actuator. Finally, we show that a simple linear model adequately captures the input-output dynamics of the actuated flow—a promising result for future implementation in active control systems.

DOI: [10.1103/PhysRevFluids.7.114101](https://doi.org/10.1103/PhysRevFluids.7.114101)

I. INTRODUCTION

Developing our ability to actively control fluid flows would allow engineers to improve real-world systems and supply researchers with tools to further probe the underlying dynamics of these systems. Consequently, the field of active flow control has received considerable attention in the last several decades [1–3]. Despite these efforts, many areas of the field still require significant progress if we are to implement active flow control strategies into real systems in a robust and meaningful way. The present work focuses on one aspect of the problem: our ability to manipulate fluid flows using actuators. As concluded in the review by Cattafesta and Sheplak [4], “the future is bright for active flow control, but the search for the perfect actuator continues.” This statement remains true a decade later, and so further development and study of these actuators is necessary to progress the overall field of active flow control.

In the present work we focus on an actuator that has been developed for the control of wall-bounded flows. The most popular actuators for such an application have been those that can easily be implemented into a surface while retaining some authority over the flow at a distance. In the

*ghaemi@ualberta.ca

past these have been primarily fluidic actuators (blowing/suction, jets, oscillators, etc.) and plasma actuators. Both classes of actuators have been heavily investigated in the literature and feature their own unique advantages and disadvantages. These classes of actuators are not the primary topic of the present work, and so the reader is referred to the relevant reviews of fluidic actuators [4–7] and plasma actuators [4,8–10] for more details. Instead, we focus on a class of actuators that has been relatively underdeveloped to date: deformable surface actuators. The goal with a deformable surface actuator is to manipulate the flow by dynamically changing the local geometry of the surface itself. More specifically, we are interested in actuation using smooth surface deformations applied dynamically in the wall-normal direction with the goal of locally targeting flow features directly above the surface.

It is necessary to mention that there exists a body of literature aimed at achieving a specific control outcome using open-loop forms of wall-normal deformation. These works focused primarily on controlling flow separation [11–17] and the implementation of surface waves for drag reduction [18–29]. These investigations were concerned with how surface deformations applied over large areas influence bulk flow characteristics. In contrast, we are interested in how local wall-normal deformations can be used to target specific flow features and therefore the results from these studies will not be discussed in detail. Additionally, other forms of wall-normal surface actuation that cannot be considered smooth deformations have been investigated. For example, the use of flush-mounted piezoelectric cantilevers [30–38] and some forms of dynamic roughness [39–49]. These studies will also not be discussed in detail since they are quite different from what is considered here.

The earliest work that is relevant to the present investigation showed that local surface deformations can produce high- and low-speed streamwise velocity fluctuations within laminar [50,51] and turbulent boundary layers [52] using deformations with relatively simple geometries (circular or rectangular). The results of these studies indicate that upward surface deformations produce low-speed motions while downward deformations produce high-speed motions. Kim *et al.* [52] also found that their wall-normal deformations produced streamwise vortices under certain conditions, which is similar to the result obtained by Dearing *et al.* [53] using active dimples in a laminar boundary layer. Both Kim *et al.* [52] and Dearing *et al.* [53] employed circular surface deformations at a constant amplitude of 0.1 times the actuator diameter. However, the frequencies considered by Dearing *et al.* [53] were 1-2 orders of magnitude higher than those considered by Kim *et al.* [52] if the frequency is normalized using the actuator diameter and freestream velocity. The results from these two studies suggest that higher frequencies are more likely to produce streamwise vortices, although it is probable that the amplitude and geometry of the deformation also play significant roles. The simulations of Carlson and Lumley [54] showed that an outward Gaussian deformation could be used to push streaky structures away from the surface, resulting in the expansion of the opposite-signed streaks that are adjacent to the one being targeted by the deformation. They found that the expansion of these adjacent streaks can lead to both decreases and increases in drag depending on their sign of fluctuation, thus highlighting a possible mechanism for flow control.

In contrast to studying deformations with simple geometries, Endo *et al.* [55] and Kang and Choi [56] conducted simulations wherein the local deformation of the surface beneath wall-bounded turbulence at low Reynolds numbers was set based on the flow above it. Both investigations reported drag reduction, but the resulting surface deformations were highly complex since each element of the surface could be deformed at will. This complexity is not practical for physical implementation, which is why Endo *et al.* [55] also considered an array of streamwise-elongated deformations that responded to upstream shear measurements. This arrangement manipulated the near-wall streaks and produced a net positive energy savings, thus providing another example of relatively simple surface deformations being used to target streaky structures. More recently, the investigations of Pamiès *et al.* [57], Zhang *et al.* [58], and Ge *et al.* [59] considered similar simulations but using active dimples and pimples. These studies were less successful than Endo *et al.* [55] at producing drag reduction, suggesting that the particulars of a wall-deformation control strategy are critical to its success. Finally, Goldin *et al.* [60] demonstrated the delay of disturbance growth in a laminar boundary layer using wall-normal surface deformations generated using a series of bars attached

to a flexible membrane. This work focused on the implementation of a model predictive controller, and so the associated velocity field was not thoroughly measured. Despite this, the work represents a successful experimental demonstration of active control using wall-normal surface deformations.

As we have seen above, the idea of using local wall-normal surface deformations as a means of actuation for flow control has been around for a few decades. Although there is clear interest in the topic, the actuation concept has received far less attention when compared to more popular options such as fluidic and plasma actuation. As a result, the literature lacks the information necessary for designing a suitable surface deformation for targeting a given flow feature in a control application. More specifically, it is not clear how the frequency and amplitude of simple surface deformations affect the motions that are produced. This information is critical for determining which features of a flow can be effectively targeted using this actuation strategy. We have therefore developed an actuator capable of producing circular surface deformations similar to those considered by Carlson and Lumley [54], Kim *et al.* [52], and Dearing *et al.* [53]. We refer to this device as the *active surface*, and we have deployed it beneath a laminar boundary layer to expand upon the sparse literature regarding how simple wall-normal surface deformations influence wall-bounded flows. The laminar boundary layer was selected for two reasons: (i) it is the simplest wall-bounded flow and is therefore the logical choice for an initial evaluation of a new actuator in a *clean* flow, and (ii) it allows us to easily evaluate models for the input-output dynamics of the actuated flow because the unactuated flow is steady.

We begin by detailing the design of the active surface and the characteristics of the surface deformations it produces. We then consider how periodic surface deformations influence the flow over a range of actuation amplitudes and frequencies with an emphasis on the spatial structure, strength, and stability of the resulting motions. Finally, we show that a simple linear model that is commonly used to design controllers is capable of capturing the input-output dynamics of the actuated flow.

II. EXPERIMENTAL SETUP

The performance of the active surface has been experimentally evaluated using high-speed particle image velocimetry (PIV) in the two-story wind tunnel facility at the University of Alberta. The test section has dimensions of $2.4 \text{ m} \times 1.2 \text{ m} \times 11 \text{ m}$ ($W \times H \times L$), the upstream transition to the test section features a contraction ratio of 6.3:1, and the side walls are made from transparent acrylic to allow optical access for the PIV measurements. The active surface was placed beneath a laminar boundary layer formed over a flat plate located mid-way down the length of the test section. The plate, which is shown schematically in Fig. 1, was machined from aluminum and features a smooth surface finish. It has a thickness of 12.7 mm, a length of 123 cm, and a width of 100 cm. The trailing edge is sharp and the leading edge is the profile from Hanson *et al.* [61] which has been optimized for experimental studies of laminar boundary layers. The plate was modified to accommodate the active surface such that its center was located 17.5 cm from the leading edge at center span. The active surface sits flush with the plate and the gaps between the two components were filled with a malleable polymer clay to achieve a smooth transition. The plate was supported in the freestream using adjustable feet such that the surface over which the boundary layer formed was roughly 20 cm from the bottom wall of the test section. This was well above the height of the boundary layer that forms along the test section walls. The wind tunnel was operated at a free stream velocity of $U_\infty = 4.0 \text{ m/s}$, which is slow enough to produce a laminar boundary layer but fast enough to maintain a steady freestream with low turbulence intensity. Considering the freestream velocity and the location of the plate in the test section, the turbulence intensity was around 0.5% [62] and the mean freestream velocity remained uniform within $\sim 1\%$ across the span [63,64]. A Cartesian coordinate system is used and the origin is placed at the center of the undeformed active surface as is shown in Fig. 1. The streamwise, wall-normal, and spanwise directions are denoted with x , y , and z , respectively. The associated velocity components are U , V , and W with fluctuating

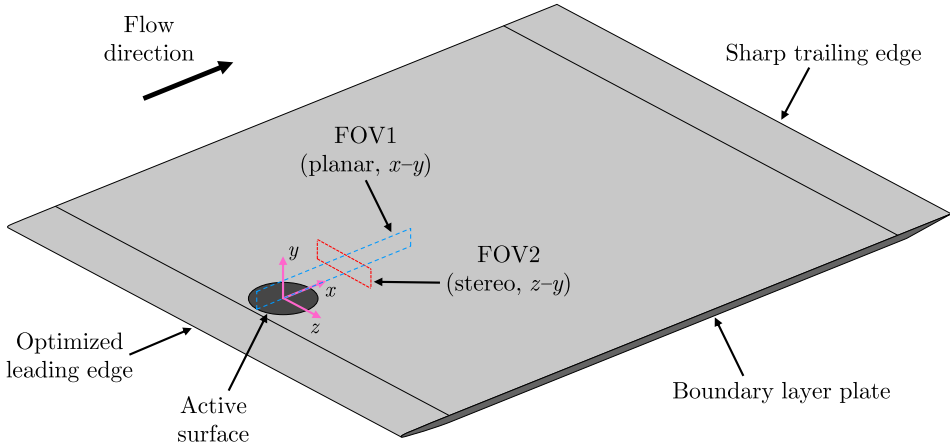


FIG. 1. Schematic of the experiment showing the boundary-layer plate, active surface, and fields of view used for PIV.

components u , v , and w . The height of the active surface deformation in the wall-normal direction is denoted as h .

A. Active surface design

The active surface assembly is a circular insert that can be fastened flush to the upper surface of the flat plate as is shown in the cross-sectional schematic of Fig. 2(a). The primary feature of the assembly is a circular disk of smooth silicone rubber that can be deformed in the wall-normal direction using a linear actuator. The rubber features a thickness of 1.52 mm, a 50A Shore hardness, and is rated for high temperatures so that the high-speed PIV laser does not heat and damage the surface during experiments. The portion of the flexible disk that is free to deform has a diameter of $D = 100$ mm as is shown in Fig. 2(a); the portion of the disk beyond this diameter is attached to the insert using an adhesive while retaining some tension in the material so that it does not sag where it is unsupported. The flexible disk is driven from underneath by a smaller rigid disk with a diameter of $d = 50$ mm. The rigid disk is attached to the linear actuator on one end using threads

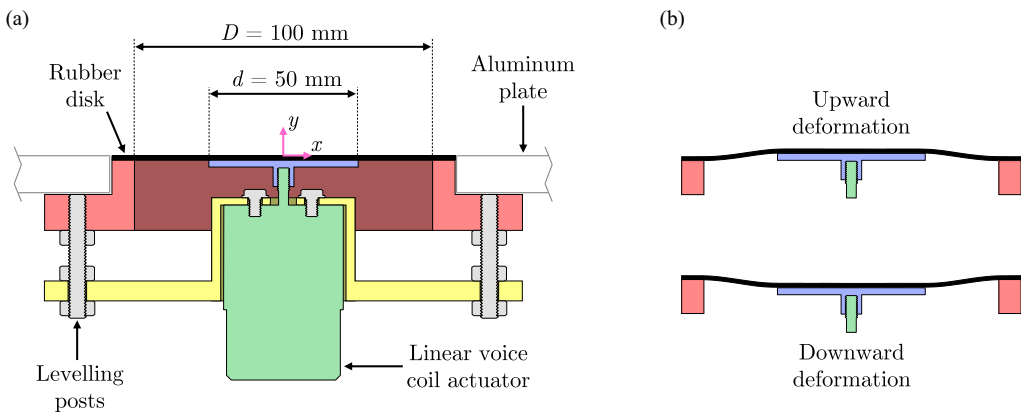


FIG. 2. Cross-sectional schematics of (a) the active surface assembly and (b) the upward and downward surface deformation. Note that the assembly is circular and therefore the deformation is axisymmetric.

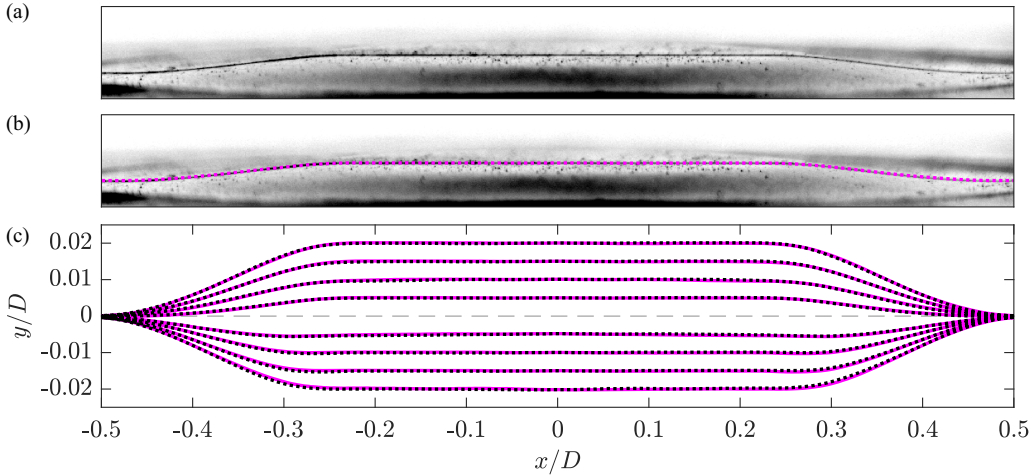


FIG. 3. (a) Sample photograph (intensity inverted for clarity) showing the deformed surface at a displacement of 2.0 mm, (b) the same photograph with the extracted profile overlaid using a dotted line, and (c) all measured profiles of the deformed surface at displacements of ± 0.5 mm, ± 1.0 mm, ± 1.5 mm, and ± 2.0 mm. In panel (c), the vertical axis has been stretched by a factor of four to better show the profiles and the dotted lines are the same profiles flipped about $x = 0$ to highlight the symmetry of the deformation.

and is attached to the flexible disk on the other end using an adhesive. Leveling posts allow for fine adjustment of the actuator location with respect to the flexible disk to ensure the surface is flat at zero displacement ($h = 0$).

A linear voice coil actuator (BEI Kimco LAS16-23-000A-P01-4E) featuring an integrated position sensor has been selected to actuate the flexible disk. This linear actuator is capable of maximum displacements of ± 3.04 mm at frequencies up to 117 Hz (sinusoidal) according to the manufacturer data sheet. However, the linear actuator must accelerate the mass of the disks and also work against the tension of the flexible surface and the force of gravity. As a result, the maximum actuation frequency achieved here is 40 Hz and the maximum displacement considered is ± 2.0 mm. The actuator is powered using an external power supply and controlled using a servo drive that has been programmed using Ingenia MotionLab software. The displacement of the actuator can be read from the integrated position sensor and the desired displacement can be set using an external voltage signal. These signals have been recorded and generated using Simulink Real-Time via a Speedgoat target machine equipped with a 16-bit input/output module (model IO135).

The shape of the active surface when it is deformed has been measured by imaging the surface from the side. Since the deformation is circular, capturing the deformation in a plane passing through the center of the active surface is sufficient. A thin silver line was drawn through the center of the surface and illuminated. A camera (the same model used for PIV, more details in Sec. II B) fitted with a 200-mm lens featuring an aperture setting of $f/4$ was used to image this line for surface deformations of $h = \pm 0.5$ mm, ± 1.0 mm, ± 1.5 mm, and ± 2.0 mm. An edge detection method was then used to extract the surface profiles from the images which were clearly highlighted by the silver line. Note that it was possible to capture the downward deformations using this technique due to the large aperture of the camera lens. A sample raw image of the surface deformation is shown in Fig. 3(a). The same image with the extracted surface profile overlaid using a dotted line is shown in Fig. 3(b) to confirm that the edge detection method does a good job of extracting the surface profile from the image. Finally, Fig. 3(c) shows the surface profiles for all considered cases. In this subfigure the dotted lines are the same profiles as the solid lines, but they have been flipped about $x = 0$ to highlight the symmetry of the deformation.

B. Particle image velocimetry

Two separate high-speed PIV experiments were conducted to capture the performance of the active surface: a four-camera planar measurement that was stitched together into a single field of view (FOV) and a stereoscopic measurement. The same cameras and laser were used for both experiments. The high-speed cameras (Phantom v611) feature a 1280×800 -pixel complementary metal oxide semiconductor sensor with a $20 \mu\text{m} \times 20 \mu\text{m}$ pixel size and 12-bit resolution. The high-speed laser (Photonics Industries DM20-527-DH) features two separate cavities, each of which is capable of producing 20 mJ per pulse at 1 kHz. The wind tunnel was seeded with $\sim 1 \mu\text{m}$ particles using a fog generator for both experiments, and all image processing was conducted using DaVis 8.4 (LaVision GmbH).

The planar PIV experiment was used to capture the flow field above and downstream from the active surface in the streamwise–wall-normal plane at center span ($z = 0$). Each camera was fitted with a $2\times$ teleconverter and a 200-mm lens featuring an aperture setting of $f/5.6$. The combined FOV, which is denoted as FOV1 within Fig. 1, has dimensions of $(\Delta x, \Delta y) = 305 \text{ mm} \times 29 \text{ mm}$ and a resolution of $64.5 \mu\text{m}/\text{pixel}$. FOV1 was stitched together from the sub-FOVs of four cameras to capture a larger extent of the streamwise direction while retaining sufficient resolution. However, the cameras viewing adjacent sub-FOVs could not be placed side-by-side while retaining FOV overlap for stitching because of the large size of each camera. As a result, the cameras viewing the first and third sub-FOVs were placed on one side of the test section and the cameras viewing the second and fourth sub-FOVs were placed on the other side of the test section. This arrangement required a transparent calibration target so that the cameras on opposite sides of the test section could view the same plane during the calibration process. The target was made in-house by printing a dotted grid of known dimensions onto a transparency film and adhering it to a flat piece of glass. The entirety of FOV1 was illuminated with a 1-mm-thick laser sheet formed using a combination of spherical and cylindrical lenses. The sheet was directed from downstream using a mirror that was located within the test section behind the boundary-layer plate.

The parameters of the data acquisition for FOV1 were the same for all cases considered. Sets of 4000 double-frame images were collected from each of the four cameras at an acquisition rate of 500 Hz, resulting in 8 s of time-resolved data for each case. The images were preprocessed in two steps. The minimum of each ensemble was subtracted to reduce the background noise, and then the images were divided by the background-subtracted ensemble average to normalize the intensity counts. The preprocessed double-frame images were then cross-correlated using a multi-pass algorithm. The final pass employed 24×24 -pixel Gaussian-weighted interrogation windows with 75% overlap. The resulting vector fields were stitched into a single FOV using the information from the target calibration, and then a post-processing round was performed. This included applying universal outlier detection [65] to detect spurious vectors, which were then replaced using polynomial interpolation in both space and time.

The stereoscopic PIV experiment was used to capture the spanwise variation of the flow field downstream from the active surface in the spanwise–wall-normal plane. Two cameras were used, each with Scheimpflug mounts, $2\times$ teleconverters, and 200-mm lenses with aperture settings of $f/16$. Both cameras were placed at 45° to the imaging plane and were arranged in a forward-scattering orientation with respect to the laser sheet. The stereoscopic FOV, which is denoted as FOV2 within Fig. 1, was located 11 cm downstream from the center of the active surface ($x/D = 1.1$). FOV2 had dimensions of $(\Delta z, \Delta y) = 122 \text{ mm} \times 28 \text{ mm}$ and an effective resolution of $70.1 \mu\text{m}/\text{pixel}$. The stereoscopic calibration included a three-dimensional target calibration followed by a self-calibration using a small set of particle images [66]. FOV2 was illuminated with a thicker 2-mm laser sheet to improve the correlation between double-frame images since the mean flow direction was normal to the imaging plane.

The same data acquisition parameters for FOV2 were used for all cases considered. Sets of 4000 double-frame images were collected from both cameras at an acquisition rate of 1 kHz, resulting in 4 s of time-resolved data for each case. A higher acquisition rate was used for stereoscopic

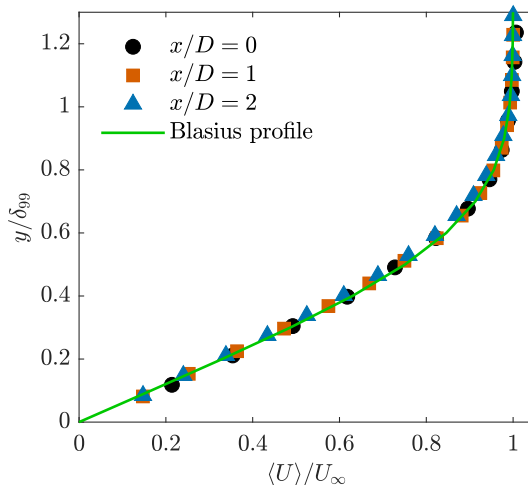


FIG. 4. Mean boundary-layer profiles for the base flow measured at three streamwise locations and compared to the Blasius solution.

PIV compared to planar PIV to improve the temporal resolution of the measurements, as the flow structures do not remain in FOV2 for long. The same image processing steps that were applied to the planar PIV images were also applied to the stereoscopic images, with the only differences being that the multi-pass cross correlation was the stereoscopic variant of the algorithm and 32×32 -pixel Gaussian-weighted interrogation windows were used.

Finally, the trigger signals for the laser and cameras were recorded along with the actuator signals during all PIV experiments. This was done so that the resulting vector fields could be synchronized with the displacement of the active surface for analysis purposes. These signals were recorded via Simulink Real-Time using the same target machine that was used to operate the actuator.

C. Base flow

The mean velocity profiles at $x/D = 0, 1,$ and 2 for the base flow are presented in Fig. 4 where $\langle \dots \rangle$ denotes an ensemble average and δ_{99} is the boundary-layer thickness based on $0.99U_\infty$. It is evident in the figure that the velocity profiles closely match the Blasius solution at all three streamwise locations, confirming that the laminar boundary-layer plate produces the desired flow field. The boundary-layer thickness (δ_{99}), displacement thickness (δ^*), momentum thickness (θ), and the Reynolds number computed using the displacement thickness (Re_{δ^*}) at the same three streamwise locations are given in Table I. Note that $\text{Re}_{\delta^*} = 520$ at $x/D = 2$ coincides exactly with the “indifference point” for the Blasius profile [67]. This is the largest Reynolds number that can be achieved before neutral disturbance waves, which are periodic in both space and time [68], begin to

TABLE I. Boundary-layer parameters for the base flow at three streamwise locations: boundary-layer thickness at $0.99U_\infty$ (δ_{99}), displacement thickness (δ^*), momentum thickness (θ), and the Reynolds number computed using the displacement thickness (Re_{δ^*}).

x/D	δ_{99} [mm]	δ^* [mm]	θ [mm]	Re_{δ^*}
0	4.1	1.4	0.5	340
1	5.3	1.9	0.7	450
2	6.0	2.2	0.8	520

amplify within the laminar boundary layer according to linear stability analysis. The present study was designed to place this point sufficiently downstream from the active surface to decrease the chance that the forcing causes an immediate transition to turbulence. However, as we will discuss later in Sec. III B, the periodic motions produced by the active surface can become unstable prior to this point.

D. Actuation cases

Two types of actuation were considered in the present investigation: periodic and random deformation of the active surface. Periodic deformation was considered to investigate how the amplitude and frequency of active surface deformations affect the flow field. We operated the actuator using the signal

$$h_r(t) = A \sin(2\pi f_a t), \quad (1)$$

where A is the actuation amplitude, f_a is the actuation frequency, t is time, and h_r is the reference signal in millimeters that is meant to be tracked by the actuator. We considered amplitudes of 0.5, 1.0, 1.5, and 2.0 mm, which correspond to 12% to 49% of the local boundary-layer thickness, and frequencies ranging from 4 to 40 Hz in increments of 4 Hz. The actuation amplitudes and frequencies are normalized using the active surface diameter $D = 100$ mm and the freestream velocity $U_\infty = 4.0$ m/s throughout most of this paper. In the case of the normalized frequency this produces the Strouhal number $St = f_a D / U_\infty$. The normalized values therefore range from $A/D = 0.005$ to 0.02 and $St = 0.1$ to 1.0 . Finally, we consider a randomized $h(t)$ signal as the second type of actuation. This was done for the purposes of system identification; more details regarding this randomized signal and its use are discussed in Sec. IV.

The results from the periodic deformation cases constitute the primary data in the present investigation. The desired displacement of the active surface was specified using the reference signal given by Eq. (1) for these cases. We found that the amplitudes of the measured displacement signal were typically within a few percent of the desired value. It is also important to note that the measured displacement only captures the motion of the flat portion of the deformation as set by the small rigid disk that is directly fixed to the linear actuator. The behavior of the unsupported portion of the active surface should also be considered, as high frequencies and amplitudes could cause this portion of the surface to experience secondary oscillations depending on the properties of the material. To show that this is not a significant concern for the present investigation, we have recorded high-speed videos of the active surface operating at the maximum amplitude of 2 mm and actuation frequencies of 20 and 40 Hz. These recordings are shown in Movies 1 through 4 in the Supplemental Material [69], and they reveal that any secondary oscillation of the unsupported portion of the active surface is small in comparison to the primary deformations and only occurs at the highest frequencies.

E. Phase averaging

A phase-averaging technique was applied to the vector fields associated with the periodic deformation cases to obtain improved representations of the resulting periodic flows. We found that these phase-averaged velocity fields are an excellent representation of the instantaneous flow when the motions downstream from the active surface remain periodically organized. However, phase averages of the actuation cases that result in a transition to turbulence no longer provide a good representation of the flow beyond the point of transition. This did not pose any issues for us since we are not interested in the flow downstream from a transition to turbulence. Moreover, the phase-averaged flow fields of the cases featuring transition still provide useful information. For example, they show the structure and strength of the motions leading up to transition and also the streamwise location at which transition occurs (as indicated by abrupt changes in the structure and strength). For these reasons we focus on the phase averages throughout our analysis of the periodic deformation cases.

The phase of the active surface ϕ was extracted from the measurements of h using a Hilbert transform as

$$\phi = \angle[-i\mathcal{H}(h)] + \pi, \quad (2)$$

where $\mathcal{H}(h)$ denotes the Hilbert transform of the active surface displacement. The manipulations with i and π were used to shift the phase such that one full cycle extends from $\phi = 0$ to 2π with $\phi = 0$ representing the active surface at $h = 0$ with a velocity in the positive wall-normal direction. The velocity fields were averaged using phase bins with widths of 0.1π and 80% overlap. Since each set contains 4000 measurements, each average was computed using roughly 200 vector fields.

III. MOTIONS PRODUCED BY PERIODIC FORCING

In this section we evaluate how the active surface influences the laminar boundary layer when operated according to the periodic actuation cases discussed in Sec. II D. We focus on the spatial structure, strength, and stability of the periodic motions that form as a result of the active surface deformations. We consider only the streamwise velocity fluctuations, as we found that the phase averages of v are roughly five to ten times weaker than the phase averages of u (prior to instability growth).

A. Spatial structure of the actuated motions

We begin by studying the spatial structure of the motions that result from operating the active surface to produce periodic deformations. In general, the structure of the flow under these conditions can be characterized as modes featuring repeating high- and low-speed motions that form above the active surface and advect downstream. The high-speed motions form as the surface moves downwards and suctions high-speed fluid toward the wall, while the low-speed motions form as the surface moves upwards and pushes low-speed fluid away from the wall. The shape, dimensions, intensity, and stability of the resulting modes depend heavily on the frequency and amplitude of actuation. To begin investigating these modes we consider the flow formed from actuation at an amplitude of $A/D = 0.005$, which is the smallest amplitude considered in this study. The modes formed at this small actuation amplitude are generally more organized and stable than those formed using larger deformations of the active surface and therefore they allow us to more easily scrutinize how the modes vary as function of frequency. In fact, it is the only actuation amplitude considered here that produces modes that remain organized throughout the entirety of FOV1 for all actuation frequencies. As a result, the phase averages of these cases are an excellent representation of the instantaneous flow field.

Phase averages of the fluctuating streamwise velocity ($\langle u \rangle_\phi$) are given in Fig. 5 for all actuation frequencies considered at an amplitude of $A/D = 0.005$. A phase of $\phi = 3\pi/2$ is shown in all cases, which corresponds to the surface being at the lowest position of the cycle with zero velocity. All panels within the figure show a series of high- and low-speed motions that alternate in the streamwise direction. The height of these motions remains relatively constant at around $0.05D$ ($\sim \delta_{99}$), but their wavelengths in the streamwise direction are a strong function of the actuation frequency. As the frequency is increased from $St = 0.1$ to 0.3 [Figs. 5(a)–5(c)], we see a rather drastic reduction in the length of the high- and low-speed motions while the mode shape remains similar overall. When the actuation frequency reaches $St = 0.4$ [Fig. 5(d)] we see a break in this trend. The flow structures are now relatively weak, and the structure immediately downstream from the active surface has a positive sign of fluctuation—the opposite of what is observed for $St = 0.1$ to 0.3 . We then see a return to the original mode shape as the frequency is increased through the range $St = 0.5$ to 0.9 [Figs. 5(e)–5(i)], where the streamwise wavelengths of the modes continue to decrease as frequency is increased. Finally, we see a break in the trend once again for $St = 1.0$ [Fig. 5(j)], which appears to generate the same mode shape that was observed at $St = 0.4$ but with a reduced streamwise wavelength. Overall, it appears that there are alternating transitions between

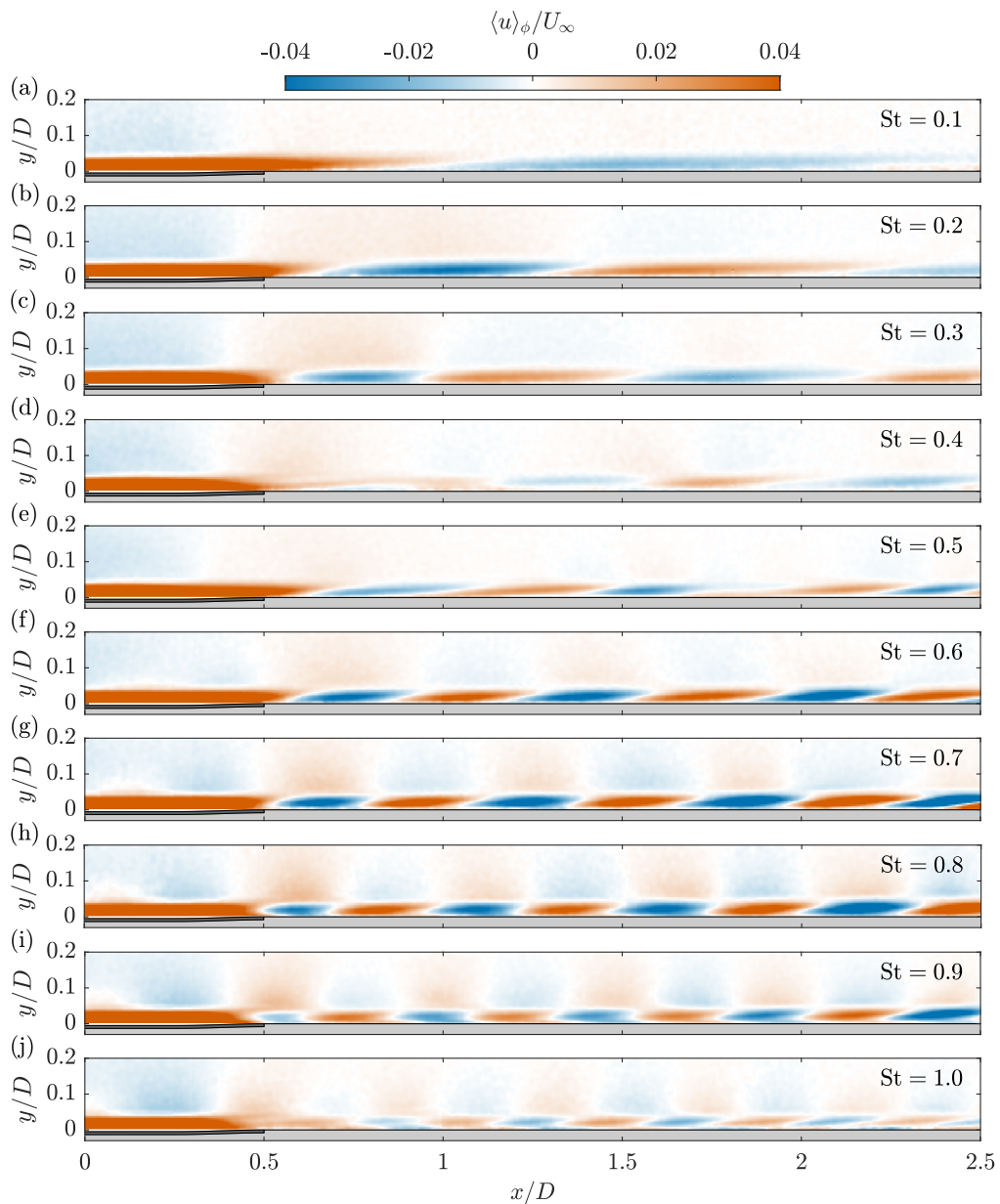


FIG. 5. Phase averages of the fluctuating streamwise velocity ($\langle u \rangle_\phi$) within FOV1 ($z = 0$) resulting from periodic surface deformation at an amplitude of $A/D = 0.005$. Panels (a–j) coincide with actuation frequencies of $St = 0.1$ through 1.0 . The phase of the deformation is $\phi = 3\pi/2$ in all cases, i.e., the surface is at the lowest position of the cycle with zero velocity.

two different mode types as St is increased. These mode types are maintained at the higher actuation amplitudes, although they are more intense and therefore less stable; this will be discussed in more detail in Sec. III B.

To further investigate the modes visible in Fig. 5 we consider their streamwise wavelengths (λ_x), i.e., the streamwise distance between motions with the same sign of fluctuation. These wavelengths

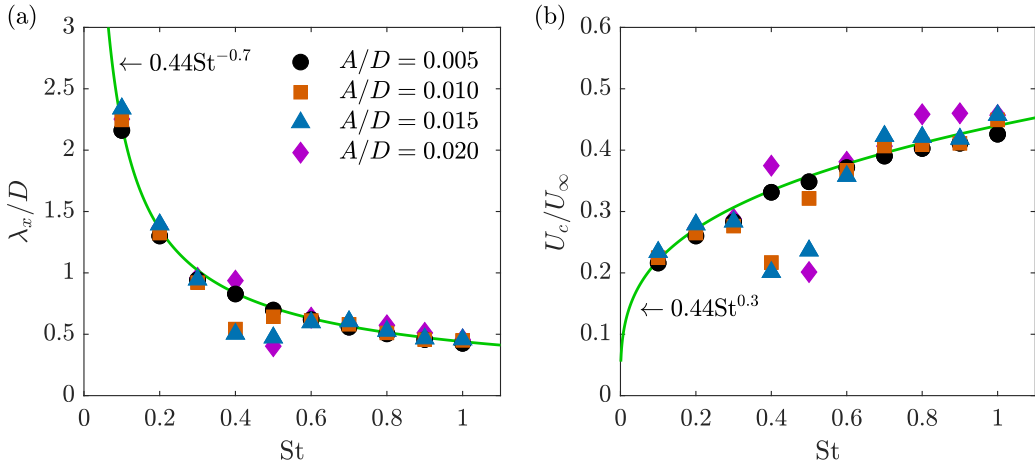


FIG. 6. (a) The streamwise wavelength (λ_x) of the modes produced by periodic deformation of the active surface and (b) the associated advection velocities of the modes computed as $U_c = f_a \lambda_x$.

were computed by applying an autocorrelation in the streamwise direction to an isolated portion of the instantaneous snapshots of streamwise velocity fluctuation that contains the periodic modes. The average of all 4000 autocorrelation curves for each case was used to extract the wavelength by locating the point at which the autocorrelation curve reaches a minimum. This point is half the wavelength because it occurs when the autocorrelation has been shifted such that adjacent structures with opposite sign of fluctuation overlap. To isolate the modes for the autocorrelation, we extracted the portion of each snapshot beyond $x/D = 0.5$. The height of the extracted portion was limited to $y/D = 0.1$, and the length was limited to $0.75\hat{\lambda}_x$ where $\hat{\lambda}_x$ is the streamwise wavelength estimated from the phase averages of Fig. 5. This was done to capture the streamwise extent necessary for achieving the minimum of the autocorrelation function without including the breakdown of the modes that can occur downstream for some of the larger actuation amplitudes.

The streamwise wavelengths of the modes produced by periodic actuation are presented in Fig. 6(a), where the values can be seen to range from roughly $\lambda_x/D = 2.3$ at $St = 0.1$ to $\lambda_x/D = 0.5$ at $St = 1.0$. The figure reveals that the wavelength follows a power law that is proportional to $St^{-0.7}$, thus confirming the strong dependence on the actuation frequency that is visible in Fig. 5. As a result of this power law, the wavelengths reduce quite quickly at the lower frequencies and then level off to a more gradual decline as frequency is increased. The actuation amplitude does not appear to have a large impact on the wavelength, with the exception being actuation at $St = 0.4$ and 0.5 , which reveals wavelengths that no longer agree with the power law for a few actuation amplitudes. This seems to be associated with the emergence of the new mode type at this actuation frequency, although the same behavior is not observed for the wavelengths at $St = 1.0$ where the new mode type is also found.

Since the actuation frequencies are known, we can use the wavelengths shown in Fig. 6(a) to estimate the advection velocity (U_c) of each mode using the relation $U_c = f_a \lambda_x$. These advection velocities have been computed for all cases and are presented in Fig. 6(b) along with the associated power law. The advection velocity can be seen to increase with actuation frequency, and the values range from roughly $U_c/U_\infty = 0.2$ to 0.45 . Since $U_c/U_\infty < 1$ for all cases, the modes feature a so-called ‘‘critical layer’’ centered upon the wall-normal location where the advection velocity of the mode matches the local mean velocity [68]. The analysis of these critical layers originates from linear stability theory and will be discussed in more detail in Sec. III B.

The advection velocities can be used along with Taylor’s hypothesis to transform the time domain of time-resolved measurements into a spatial domain in the streamwise direction. When used with

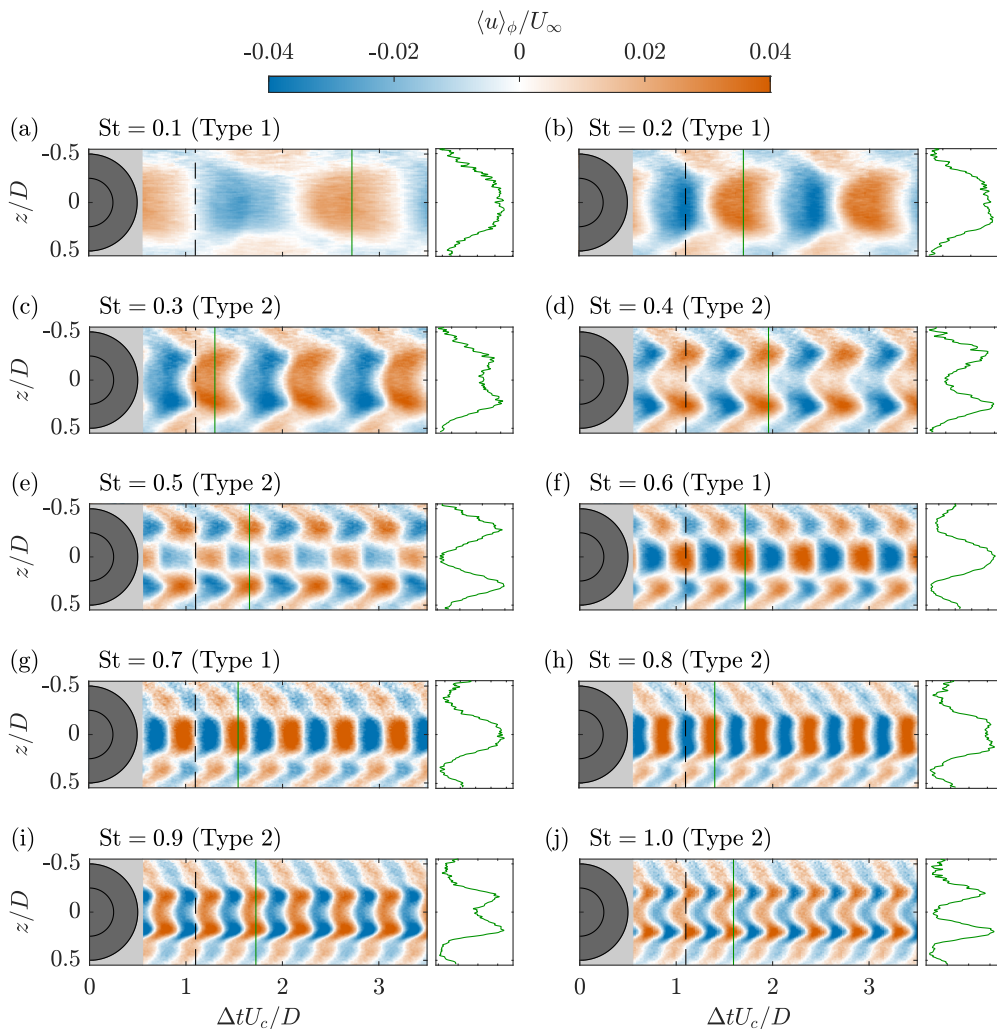


FIG. 7. Phase averages of the fluctuating streamwise velocity ($\langle u \rangle_\phi$) at a height of $y/D = 0.02$ resulting from periodic actuation at $A/D = 0.005$. Panels (a–j) coincide with actuation frequencies of $St = 0.1$ through 1.0 . The phase of actuation is $\phi = 3\pi/2$ in all cases, which is the same phase shown in Fig. 5. The streamwise axes have been formed by applying Taylor’s hypothesis using the advection velocities computed from the power law shown in Fig. 6(b). The dashed lines at $x/D = 1.1$ show the location of the stereoscopic measurements (FOV2) that were used to form these visualizations. The solid green lines show the location of the extracted velocity profiles at the right of each panel.

the stereoscopic measurements in the z - y plane of FOV2, this allows us to estimate how the motions shown in Fig. 5 vary in the spanwise direction. This transformation has been applied to the phase-averaged measurements from FOV2 at $A/D = 0.005$ while using the power law relation shown in Fig. 6(b) to compute U_c (the computed values for U_c agree well with the power law for this actuation amplitude); the results are shown in Fig. 7 for the streamwise–spanwise plane at $y/D = 0.02$. Note that these visualizations lose accuracy as we move farther away from the location where the measurements were conducted. In the present case the measurements were conducted within FOV2 at $x/D = 1.1$, and this location is marked using a dashed line in the panels of Fig. 7.

The visualizations of the motions in the streamwise–spanwise plane shown in Fig. 7 reveal interesting behavior that is not observed within the streamwise–wall-normal plane of FOV1. More specifically, we see a significant variation of the velocity fluctuations in the spanwise direction that provides insight into the true structure of the flow field downstream from the active surface for varying actuation frequencies. We can see that the different mode types really are quite distinct from one another. Some modes, for example those produced at $St = 0.4$ and 1.0 [Figs. 7(d) and 7(j)], have split down the centerline of the active surface ($z = 0$) to produce two separate motions displaced in the spanwise directions. This is clearly why these modes appear to be significantly weaker in Figs. 5(d) and 5(j). In contrast, other actuation frequencies produce modes featuring single dominant motions concentrated along the centerline of the active surface, for example $St = 0.1$ and 0.6 [Figs. 7(a) and 7(f)]. Following these observations we define the *type-1* modes as those featuring high- and low-speed motions with single maximums and minimums along $z = 0$. In contrast, we define the *type-2* modes as those featuring high- and low-speed motions with double maxima and minima displaced in the spanwise directions. Consequently, the mode types can be identified by plotting a velocity profile across the span near the location of maximum or minimum velocity fluctuation. Such profiles are shown in the subpanels of Fig. 7, revealing that actuation at $St = 0.1, 0.2, 0.6,$ and 0.7 produces type-1 modes while the remaining St produce type-2 modes. The profiles for the type-2 modes are “M-shaped,” which was also reported by Kim *et al.* [52] for $St = 0.3$.

Considering the motions produced by periodic actuation, we can conclude that it is the type-1 modes that are most desirable for flow control applications that rely on targeting individual coherent motions. This is because these modes feature dominant motions that are concentrated along $z = 0$. It is typical to place sensors and actuators aligned in the streamwise direction, and so an actuator that produces its strongest effect along its own centerline is preferable. The present active surface produces type-1 modes for $St = 0.1$ to 0.2 and $St = 0.6$ to 0.7 . The former frequency range produces velocity fluctuations that are nearly as wide as the active surface, while the latter range produces fluctuations that are much narrower. The type-1 modes produced at low frequencies are therefore a more efficient use of the space taken up by the active surface.

B. Strength and stability of the actuated motions

In the previous section we investigated the spatial structures of the modes produced by the active surface for varying actuation frequencies. We will now explore the strength and stability of these modes as a function of both actuation frequency and amplitude. The spatial structure of a mode produced at a given actuation frequency does not change significantly as the actuation amplitude is increased (prior to the breakdown of a mode via instabilities). Instead, the velocity fluctuations become stronger, which results in the mode becoming less stable overall. To first illustrate this qualitatively we consider instantaneous visualizations of the motions produced at $St = 0.7$ (type-1 mode) for all amplitudes considered. These visualizations are shown in Fig. 8 where the actuation phase remains constant for all cases to facilitate comparison. Note that proper orthogonal decomposition (POD) by the method of snapshots [70] was applied to reduce the PIV noise for the purpose of improving these visualizations. The POD reconstructions retain a minimum of 85% of the fluctuating energy.

The instantaneous visualization for $A/D = 0.005$ [Fig. 8(a)] is consistent with the phase averages shown in Figs. 5(g) and 7(g). This is because this small actuation amplitude is not large enough to cause the mode to break down within the FOV and therefore the periodicity is retained. However, while the mode remains organized, we can see that the high- and low-speed motions are increasing in strength with downstream distance. This suggests that the mode is unstable and may grow to the point of decomposition at some point farther downstream. When the actuation amplitude is increased to $A/D = 0.01$ [Fig. 8(b)], we can see that the mode now begins to break down within FOV1 as is evidenced by the high- and low-speed motions overlapping with one another near $x/D = 1.8$. It seems that this may be the natural progression of these modes when the strength of the fluctuations surpasses some threshold since high- and low-speed motions that alternate in the

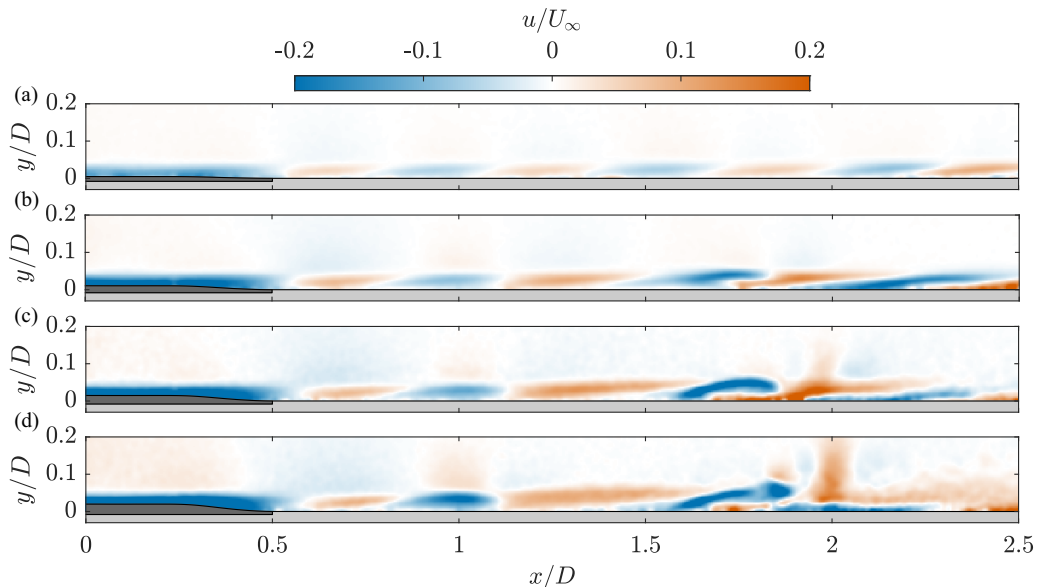


FIG. 8. Instantaneous visualizations of streamwise velocity fluctuation (u) produced at an actuation frequency of $St = 0.7$ for actuation amplitudes of (a) $A/D = 0.005$, (b) $A/D = 0.01$, (c) $A/D = 0.015$, and (d) $A/D = 0.02$. The phase of the actuator is roughly $\phi = \pi/2$ in all cases, i.e., the surface is at the highest position of the cycle with zero velocity.

streamwise direction would have a tendency to approach one another as a result of their different advection velocities. Once the actuation amplitude is further increased to $A/D = 0.015$ or 0.02 [Figs. 8(c) and 8(d)] it is clear that the coherent structures have begun to break down into smaller motions within the FOV.

All motions shown in Fig. 8 are quite similar to one another up to roughly $x/D = 1.3$. Although the height of the surface deformation has increased fourfold across the cases considered, the height of the high- and low-speed motions just downstream from the active surface does not change much. Instead, increasing the amplitude of the surface deformation increases the strength of the motions. This is most obvious when looking at the low-speed motion located around $x/D = 1$ in each panel of Fig. 8, which can clearly be seen to increase in strength as the actuation amplitude is increased. In fact, it appears that it is these low-speed motions that initiate the breakdown of the mode, as they are observed to lift up and eventually participate in the emergence of the turbulent motions as can be seen in Figs. 8(c) and 8(d). These low-speed motions will produce an inflection point within the instantaneous boundary-layer profile; such an inflection point is well-known to be associated with instability [67,71].

The instantaneous visualizations shown in Fig. 8 are generally representative of what happens to all modes when the actuation amplitude is increased. More specifically, increasing the amplitude increases the strength and decreases the stability of the motions while the spatial structure of the mode at a given frequency is roughly retained until an instability begins to grow. At the point of instability the high- and low-speed structures begin to overlap, leading to an eventual breakdown into smaller turbulent motions. Despite this generally applicable observation, these visualizations are essentially qualitative and are therefore limited in their ability to capture the full extent of the present results. To better quantify the strength and stability of the motions for all periodic actuation cases, we return to the phase averages. As described in Sec. II E, the phase-averaged results are an excellent representation of the instantaneous motions when they remain organized and periodic, but they no longer accurately represent the instantaneous flow once a mode begins to break down.

This is not an issue for the present analysis because we are interested in the strength of the periodic motions while they remain organized and whether this strength decays (stable) or grows (unstable) with downstream distance. Both pieces of information can be extracted from the phase averages and therefore they provide an excellent summary of the strength and stability of the modes produced by the active surface as a function of actuation frequency and amplitude.

The maximum absolute values of the phase-averaged streamwise velocity fluctuations [$\max(|\langle u \rangle_\phi|)$] are presented in Fig. 9 as a function of streamwise distance for all periodic actuation cases. The figure includes the measurements from both FOV1 (solid lines) and FOV2 (star symbols). The results from FOV1 consider the maximum over the wall-normal and phase dimensions along $z = 0$, while the results from FOV2 consider the maximum over the spanwise, wall-normal, and phase dimensions at $x/D = 1.1$. When these two sets of results agree (the star symbol is close to the solid line) it is because the maximum occurs near $z = 0$ (type-1 mode) and is captured by both FOVs. When a significant discrepancy is observed it is because the maximum occurs away from $z = 0$ (type-2 mode) and is therefore only captured by the measurement in FOV2. The quantity plotted in Fig. 9 provides a measure of the average peak strength of the fluctuations produced by the active surface and will simply be referred to as the *strength* of the modes to ease the discussion moving forward.

First we consider the strength and stability of the flow downstream from the active surface at the frequency and amplitude combinations that produce type-1 modes. As shown previously (Fig. 7) this occurs for $St = 0.1, 0.2, 0.6,$ and 0.7 . Since FOV1 is located at $z = 0$, the results shown in Fig. 9 are well-suited for quantifying the strength and stability of these type-1 modes. The velocity fluctuations produced by periodic deformation at $St = 0.1$ [Fig. 9(a)] appear to remain stable for amplitudes ranging from $A/D = 0.005$ to 0.015 as is indicated by the observed decay in strength with streamwise distance. In contrast, actuation at $A/D = 0.02$ produces a mode with a strength that begins to grow substantially beyond $x/D = 2$, thus indicating that the associated mode has become unstable. Similar behavior is observed for $St = 0.2$ [Fig. 9(b)], but at this frequency both $A/D = 0.015$ and 0.02 produce an unstable mode. We can also see that the points from FOV2 agree well with the curves from FOV1 for $St = 0.1$ and 0.2 , indicating that the maximum strength occurs near $z = 0$ and confirming that these are in fact type-1 modes. This is also the case for $St = 0.6$ and 0.7 [Figs. 9(f) and 9(g)]. However, these actuation frequencies appear to produce type-1 modes that are unstable for all actuation amplitudes considered. This is indicated by the strength either becoming erratic within FOV1 ($A/D \geq 0.01$) or continuing to grow with downstream distance ($A/D = 0.005$).

The strength of the type-1 modes produced at $St = 0.1$ and 0.2 for the same actuation amplitudes are quite similar if we only consider the portion of the curves prior to instability growth. If we look at the strength at the edge of the active surface ($x/D = 0.5$), then we can see that both actuation frequencies produce a maximum strength that ranges from roughly $0.1U_\infty$ to $0.35U_\infty$ as the actuation amplitude is increased [Figs. 9(a) and 9(b)]. These values then decay at similar rates with downstream distance for the cases that remain stable. Since the actuation frequency has doubled between these two cases, so has the velocity of the surface. Despite this, the strength remains similar. The same result is visible for the type-1 modes produced at $St = 0.6$ and 0.7 [Figs. 9(f) and 9(g)], i.e., the strength of the fluctuations produced at the edge of the active surface is similar for both frequencies as long as we are considering the same actuation amplitude. However, these fluctuations are weaker overall compared to those produced at $St = 0.1$ and 0.2 .

Unfortunately, the present results do not allow us to quantify the strength of the type-2 modes as well as we can quantify that of the type-1 modes. This is because the extrema have moved away from $z = 0$ and therefore the strongest velocity fluctuations occur outside of FOV1 which is where the results shown in Fig. 9 are concentrated. Despite this, the results in Fig. 9 indicate that the modes produced at higher frequencies are generally unstable while the low frequencies ($St \leq 0.2$) have higher stability. Moreover, these low-frequency modes are stronger and of type 1. Together, these characteristics suggest that low-frequency operation of the active surface is the best option for flow control.

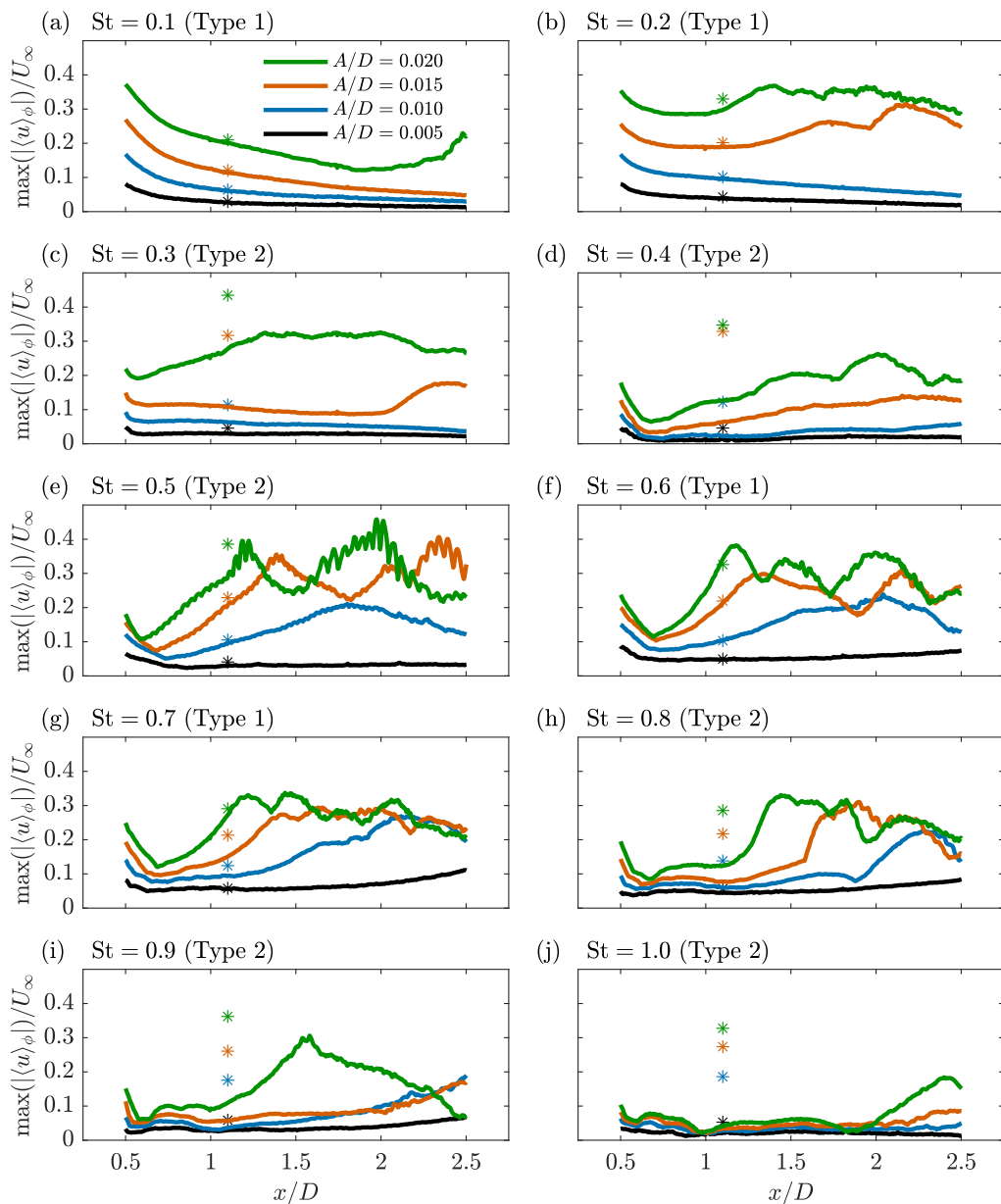


FIG. 9. Maximum absolute values of the phase-averaged streamwise velocity fluctuations (i.e., the strength of the modes) within $z = 0$ as a function of streamwise distance for all periodic deformation cases. The panels (a) through (j) coincide with actuation frequencies of $St = 0.1$ through 1.0 . The star symbols represent the same quantity extracted from the stereoscopic measurements at $x/D = 1.1$; large discrepancies between these symbols and the solid lines indicate that the velocity fluctuations are much stronger farther in the spanwise direction.

We will now briefly consider the modes produced by the active surface in the framework of linear stability analysis. Such an analysis considers neutral disturbance waves superimposed on a base flow (e.g., the Blasius profile) and their subsequent growth or decay according to a linearized

version of the Navier-Stokes equations [67]. In this context, a neutral wave is one that is periodic in both space and time [68] and must have a magnitude small enough to still be considered linear. These latter two points are where the present work deviates from the requirements of the linear analysis. The motions produced by the active surface are periodic in time but not in space since the actuator is finite in the spanwise direction. Moreover, since we are concerned with flow control we are not interested in small disturbances. Instead, we are interested in producing velocity fluctuations with large magnitudes that can potentially be used target various flow features. For these reasons we cannot expect our results to agree with those of the linear stability analysis. This is likely why we see instability prior to $x/D = 2$ where $\text{Re}_{\delta^*} = 520$, i.e., the “indifference point” for the Blasius profile [67]. However, there are still a few instances where we can make comparisons with the linear theory.

One characteristic of the linear theory is existence of a “critical layer” centered upon a critical point where the advection velocity of the disturbance matches the local mean velocity. This point causes a mathematical singularity in the inviscid analysis that can only be remedied by restoring the effect of viscosity within the critical layer, thus indicating that viscous effects are important within this layer. Similarly, the Stokes layer that forms adjacent to the wall as a result of the periodically fluctuating velocity field is a second region where viscous effects are important. Whether these two layers overlap with one another or are separated is related to the neutral stability curve for the Blasius profile [71]; overlapping layers indicates a lower-branch mode while separated layers indicate an upper-branch mode. Other characteristics of these modes include the maximum u of the mode occurring somewhere within the critical layer and a 180-degree phase shift in u occurring somewhere in the outer region of the boundary layer [40]. We can consider these characteristics to determine whether the modes produced by the present active surface are consistent with the critical-layer-type modes that arise from linear stability analysis.

The type-1 modes at $\text{St} = 0.2, 0.6$ and the type-2 modes at $\text{St} = 0.4, 1.0$ are shown in Fig. 10 along with the estimated size and locations of the Stokes (solid magenta lines) and critical (dotted black lines) layers. The type-1 modes [Figs. 10(a) and 10(c)] are strongest along $z = 0$ and have therefore been plotted using the measurements from FOV1. In contrast, the type-2 modes [Figs. 10(b) and 10(d)] have been plotted from the measurements in FOV2 via Taylor’s hypothesis since their strongest fluctuations are displaced in the spanwise directions; these latter two sub-plots contain the same data as Fig. 7 but shown in a different plane. We have estimated the thickness of the Stokes layer as $\sqrt{\nu/\pi f_a}$ [67]. The center of the critical layer is defined by the critical point (dashed black lines) where the advection velocity of the mode matches the local mean velocity. The maximum streamwise velocity fluctuation occurs within the critical layer and so we have used the location of the maxima to estimate the minimum thicknesses of the critical layers. The maximum is always located above the critical point for the present modes (this is typical of critical-layer-type modes [41]), and so the upper bounds of the estimated critical layers in Fig. 10 have been set by the maxima locations while the lower bounds are set by symmetry about the critical points.

The estimated Stokes and critical layers for $\text{St} = 0.2$ and 0.4 in Figs. 10(a) and 10(b) show clear overlap with one another, even with the critical layers being defined by a minimum thickness. This indicates that the type-1 and type-2 modes produced by actuation at the lower frequencies have structures in the streamwise–wall-normal plane that are consistent with lower-branch modes. In contrast, the estimated Stokes and critical layers for $\text{St} = 0.6$ and 1.0 in Figs. 10(c) and 10(d) are separated, which indicates that the type-1 and type-2 modes at higher frequencies have upper-branch structures. However, this particular observation is not absolute because the present critical layers were estimated using a minimum thickness, and so it remains possible that they are actually thick enough to produce overlap with the Stokes layers. Despite this, it seems likely that at least the type-2 mode at $\text{St} = 1.0$ [Fig. 10(d)] has an upper-branch structure because the estimated Stokes and critical layers are quite far apart. Finally, we can see that there is a change in the sign of streamwise velocity fluctuation somewhere in the range $y/D = 0.04$ to 0.05 for all cases shown in Fig. 10. This is characteristic of the 180-degree phase shift described earlier and is therefore another indication

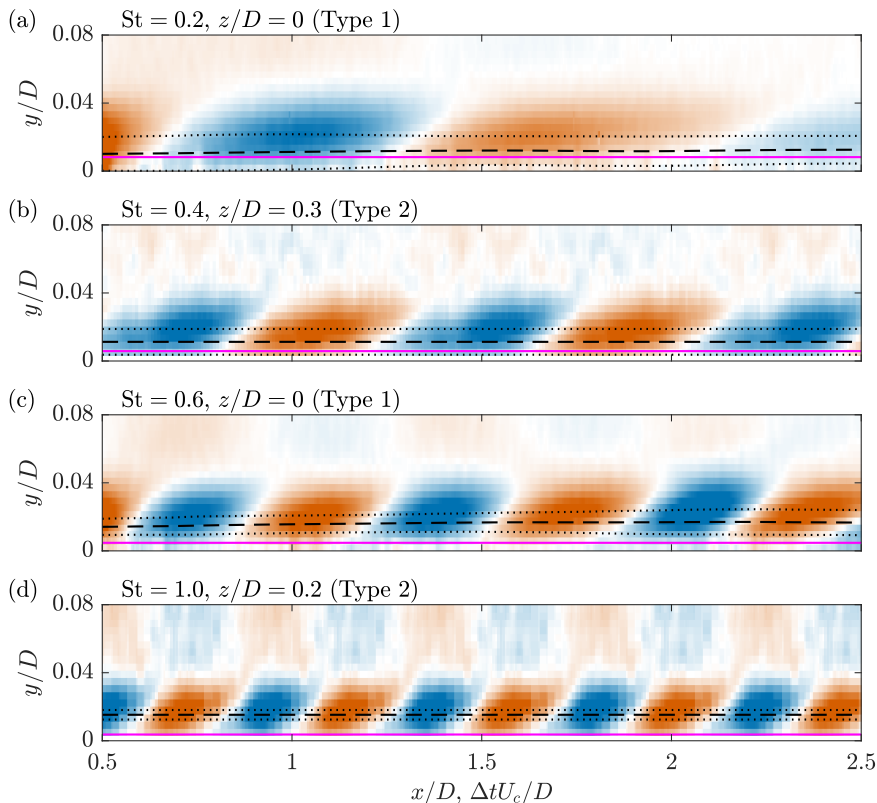


FIG. 10. Type-1 modes at (a) $St = 0.2$ and (c) $St = 0.6$ from FOV1 and type-2 modes at (b) $St = 0.4$ and (d) $St = 1.0$ from FOV2 (via Taylor's hypothesis) with the estimated location of the Stokes layers (solid magenta lines) and critical layers (black dotted lines) overlaid. The critical points (black dashed lines) are at the center of the critical layer. The wall-normal dimension is stretched here to better show the Stokes and critical layers. The colorbar scaling is the same as for Figs. 5 and 7.

that the motions produced by the active surface are consistent with the critical-layer-type modes that arise from linear stability analysis.

Considered along with Fig. 9, Fig. 10 suggests that the type-1 modes with a lower-branch structure are more stable than the type-1 modes with an upper-branch structure. Unfortunately, it is difficult to comment on the stability of the type-2 modes in the context of their critical-layer-type structures due to the spanwise location of FOV1, which does not allow for monitoring the peak strength of the type-2 modes as a function of streamwise distance.

IV. DATA-DRIVEN MODELING OF THE ACTUATED FLOW

A important aspect of any active control strategy is the model that is used to develop the controller. These models can take many forms and range from simple physics-informed heuristics to complex mathematical representations of system dynamics. One model type that is commonly applied in experimental campaigns to develop controllers for wall-bounded flows is the nonparametric linear transfer function (NLTF) (e.g., the work of Rathnasingham and Breuer [72], Juillet *et al.* [73], and Brito *et al.* [74]). This type of model is used to describe the input-output behavior of a given system and can be identified using data-driven methods. In this section, we investigate how well the input-output dynamics of the present active surface can be captured using a NLTF model.

A. Modeling with nonparametric linear transfer functions

The NLTF describes the input-output relationship between two variables in the frequency domain to the extent that this relationship can be captured by linear dynamics. In the present work we consider the input to our system to be the height of the active surface $h(t)$ and the output of the system to be the streamwise velocity fluctuation $u(t)$ at some point downstream from the active surface. The relationship between these two variables according to the NLTF model is then

$$\tilde{u}(f) = G_{hu}(f)\tilde{h}(f), \quad (3)$$

where $G_{hu}(f)$ is the NLTF between $h(t)$ and $u(t)$ while $\tilde{h}(f) = \mathcal{F}\{h(t)\}$ and $\tilde{u}(f) = \mathcal{F}\{u(t)\}$ are the Fourier transforms of the input and output, respectively. We can then employ the convolution theorem for Fourier transforms to yield

$$u(t) = g_{hu}(t) * h(t), \quad (4)$$

where the symbol “*” denotes a convolution and $g_{hu}(t)$ is the impulse response of the system. The impulse response and NLTF are therefore equivalent representations of the system dynamics and are related through the Fourier transform as $G_{hu}(f) = \mathcal{F}\{g_{hu}(t)\}$. As a result, either of these can be identified to obtain the desired model of the system.

There are numerous ways to identify either the NLTF or the associated impulse response of a system such that they are consistent with Eqs. (3) and (4). For example, the impulse response can be measured directly using an impulse response experiment. This technique is not typically used in experimental studies because it is often difficult to generate a true impulse response with a physical actuator, and this is indeed the case for the present active surface. Instead, it is typical to identify the dynamics by applying statistical approaches to randomized input-output data. One common approach employs the cross spectral density between the input and output to directly estimate the NLTF [74]. Another approach utilizes Wiener filtering to estimate the impulse response [72] which can then be used to obtain the NLTF via the Fourier transform. We have elected to use the Wiener filtering method because we found that it outperforms the spectral estimation method when applied to the present system. The application of the Wiener filter as outlined by Hayes [75] has been implemented in the present work and will be briefly detailed below.

The Wiener filter is used as an estimator whose coefficients represent the (finite) impulse response of the associated system. When this impulse response is convolved with the input to the system, it produces an optimal estimate of the output according to the minimum mean-square criterion. Since the Wiener filter is a digital filter with discrete coefficients, it is applied using sampled measurements. It should therefore be understood that $h(t)$ and $u(t)$ are considered discrete signals for the implementation of the Wiener filter moving forward. Equations (3) and (4) are still valid in discrete time and are related through the discrete Fourier transform.

The impulse response associated with the Wiener estimator is identified by solving the Wiener-Hopf equations, which are expressed using the present nomenclature as

$$\mathbf{R}_h \mathbf{c} = \mathbf{r}_{hu}, \quad (5)$$

where \mathbf{R}_h is a Toeplitz matrix containing the autocorrelations of $h(t)$, \mathbf{c} is a vector containing the filter coefficients, and \mathbf{r}_{hu} is a vector containing the cross-correlations between $h(t)$ and $u(t)$. The compact notation of Eq. (5) can be expanded to yield

$$\begin{bmatrix} r_h(0) & r_h(1) & \dots & r_h(m-1) \\ r_h(1) & r_h(0) & \dots & r_h(m-2) \\ r_h(2) & r_h(1) & \dots & r_h(m-3) \\ \vdots & \vdots & & \vdots \\ r_h(m-1) & r_h(m-2) & \dots & r_h(0) \end{bmatrix} \begin{bmatrix} c(0) \\ c(1) \\ c(2) \\ \vdots \\ c(m-1) \end{bmatrix} = \begin{bmatrix} r_{hu}(0) \\ r_{hu}(1) \\ r_{hu}(2) \\ \vdots \\ r_{hu}(m-1) \end{bmatrix}, \quad (6)$$

where m is the selected order of the Wiener filter and therefore also the length of the identified impulse response. Once a system identification experiment has been performed to obtain $h(t)$ and

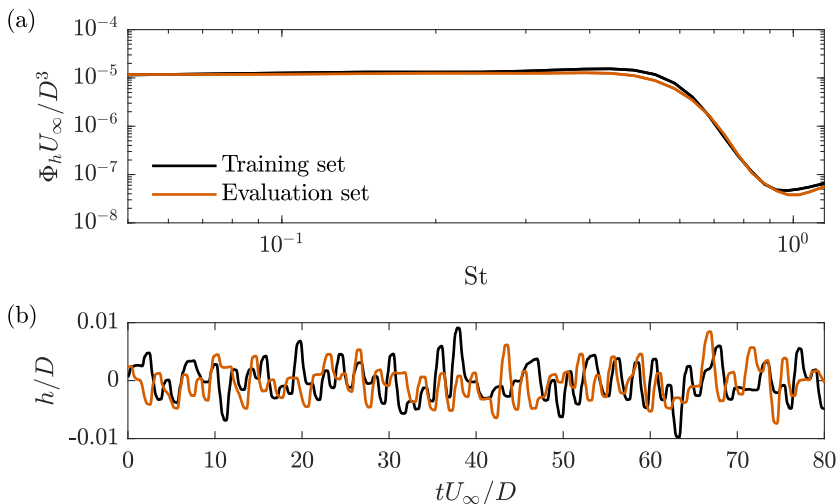


FIG. 11. (a) The PSD of the input used for system identification and model evaluation (Φ_h) and (b) samples of the corresponding time series.

$u(t)$, the above Wiener-Hopf equations can be solved to obtain the identified impulse response as $\hat{g}_{hu}(t) = \mathbf{c}$ and therefore also the associated NLTF as $\hat{G}_{hu}(f) = \mathcal{F}\{\hat{g}_{hu}(t)\}$ (the hat accents have been added to denote that these are estimates). Note that an order of $m = 250$ has been used to solve Eq. (6) in all cases presented here.

The characteristics of the input signal used in the system identification experiment are critical for achieving good results. The amplitude of the input must be large enough to elicit a response from the system, and the frequency spectrum of the input must cover the range of frequencies relevant to the application. The results from Sec. III indicate that large deformations of the present active surface result in the production of highly unstable motions. They also indicate that the lower range of the frequencies considered here seems most promising for flow control applications. We have therefore performed our system identification experiment using an input signal that halves both the frequency range and maximum deformation considered in Sec. III. More specifically, we have used an input signal that produces maximum surface deformations of $h/D = \pm 0.01$ and covers frequencies up to $St = 0.5$. Note that this frequency range contains both type-1 and type-2 modes identified in Sec. III.

Two sets of data were collected using two different input signals: one for the purpose of system identification (i.e., model training) and one for model evaluation. These two input signals were completely uncorrelated but featured nearly identical statistics. The power spectral density (PSD) of these input signals (Φ_h) and samples of the corresponding time series are shown in Fig. 11. Fig. 11(a) reveals that the PSD of both signals have almost perfect overlap. The frequency response is flat for frequencies up to $St = 0.5$, at which point a significant drop in the spectral power is observed. Fig. 11(b) shows the random nature of the input signals in the time domain and confirms that the magnitudes do not exceed $h/D = \pm 0.01$ (note that only 25% of the total input signals are shown).

The velocity fluctuations farther downstream from the active surface that are generated at lower actuation amplitudes have magnitudes on the order of a few percent of U_∞ , which is similar to the PIV noise in the present data sets. Although the system identification process discussed above ignores the uncorrelated PIV noise, this noise can still pose a problem for evaluating the performance of the NLTF model using the PIV measurements. We have therefore employed POD by the method of snapshots [70] to produce noise-reduced versions of the instantaneous velocity fields. The full details of this process are presented in the Appendix, where we demonstrate that the data reconstruction was applied carefully such that the PSD of the velocity fluctuations remains

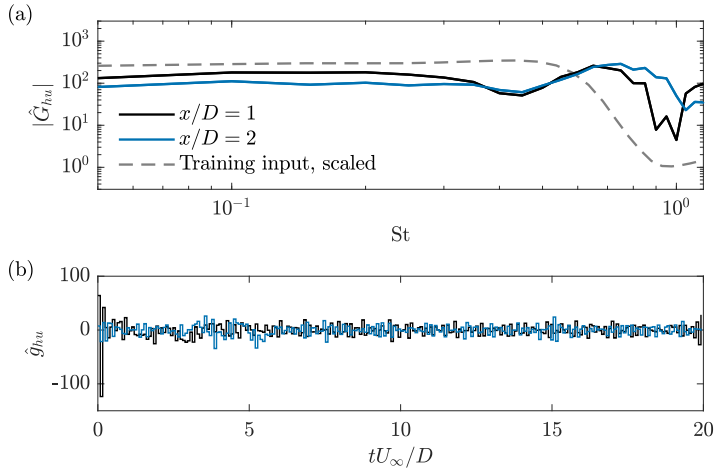


FIG. 12. (a) The magnitude of the NLTFS relating h with u at two downstream locations (extracted at $y/D = 0.03$) and (b) the associated Wiener filter coefficients which represent the impulse responses. The gray dashed line in (a) is the training input from Fig. 11(a) and is shown here (scaled) to highlight the frequency range of the NLTFS that received adequate forcing during the system identification experiment.

largely unchanged in the relevant frequency range while the noise floor is greatly reduced. This noise-reduced data has been used to both identify and evaluate the NLTFS in the present work. The streamwise velocity fluctuations have been extracted from the noise-reduced velocity fields at $y/D = 0.03$ for all cases, which is roughly the half-height of the high- and low-speed structures generated by the active surface (see Fig. 5).

The magnitude of the identified NLTFS that relate h with u at streamwise locations of $x/D = 1$ and 2 are presented in Fig. 12(a). The training input from Fig. 11(a) has been overlaid using a gray dashed line to highlight the frequency range that received significant forcing during the system identification experiment; the portions of the NLTFS that fall outside of this range will be less reliable because these frequencies were not forced adequately. Both NLTFS are relatively flat up to $St = 0.3$, at which point the magnitude begins to drop. The magnitude then starts to recover around $St = 0.5$, peaks near $St = 0.7$, and then begins to drop once again. This observed modulation of the magnitudes can be attributed to the switching between type-1 and type-2 modes that occurs with increasing actuation frequency as was discussed in Sec. III. The frequencies at which the reductions in magnitude occur are consistent with the emergence of the type-2 modes visible in Fig. 7.

The Wiener filter coefficients that represent the impulse responses associated with the NLTFS in Fig. 12(a) are shown in Fig. 12(b), where all $m = 250$ coefficients are displayed. Neither of the two impulse responses look much like those that are typical of simple linear systems, which usually oscillate and eventually damp out. Some low-frequency oscillatory behavior is observed prior to $tU_\infty/D = 5$ for both cases, but the remainder of the identified impulse responses appear quite erratic. In general, these impulse responses are difficult to interpret in a meaningful way. However, we must keep in mind that they are sets of filter coefficients meant to describe the dynamics of a nonlinear system of high dimension.

B. Model evaluation

We now move on to evaluating the estimates produced by the NLTF model. These estimates have been obtained by convolving the identified impulse responses with the input to the evaluation data set as

$$\hat{u}(t) = \hat{g}_{hu}(t) * h(t), \quad (7)$$

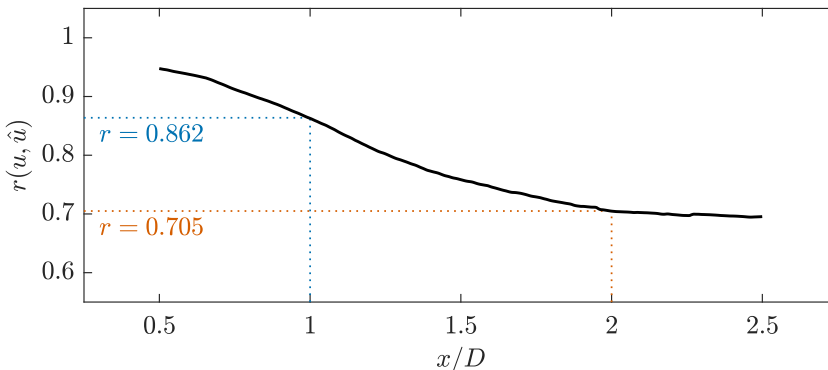


FIG. 13. The correlation coefficient between the measured (u) and estimated (\hat{u}) streamwise velocity fluctuations as a function of streamwise location. The two streamwise locations that are highlighted are the same locations for which the NLTFs and impulse responses are plotted in Fig. 12.

where $\hat{u}(t)$ is the estimated streamwise velocity fluctuation downstream from the active surface. We then compare these estimates to the velocity fluctuations measured using the POD-filtered PIV within FOV1 to determine how well the NLTF model captures the input-output dynamics of the present system.

The comparison is first made using the correlation coefficient between $u(t)$ and $\hat{u}(t)$ at all locations downstream from the active surface. This coefficient is denoted as $r(u, \hat{u})$ and is presented in Fig. 13. The results show that the correlation coefficient is $r(u, \hat{u}) = 0.95$ at $x/D = 0.5$, indicating the the NLTF model does a great job of estimating the streamwise velocity fluctuations immediately downstream from the active surface. The coefficient then begins to decline with increasing distance from the active surface, most likely due to the nonlinearity of the system. The two streamwise locations for which the NLTF models are presented in Fig. 12 are highlighted in Fig. 13, revealing correlation coefficients of $r(u, \hat{u}) = 0.86$ and 0.71 for $x/D = 1$ and 2 , respectively. Finally, the coefficient reaches a value of $r(u, \hat{u}) = 0.70$ at the end of FOV1 ($x/D = 2.5$). The decline in $r(u, \hat{u})$ can be seen to slow beyond $x/D = 2$. However, it is unlikely that this trend is sustained beyond the end of FOV1 because it only becomes more difficult for the NLTF model to capture the input-output behavior as nonlinearities grow with downstream distance. It is therefore more likely that the correlation coefficient begins to drop drastically at some point beyond $x/D = 2.5$.

The PSD and instantaneous signals of u and \hat{u} at $x/D = 1$ and 2 are presented in Fig. 14 to further compare the characteristics of the estimated and measured streamwise velocity fluctuations. The PSD of u and \hat{u} at $x/D = 1$ in Fig. 14(a) show excellent agreement over the majority of the targeted frequency range, with the exception of some small differences at the lowest frequencies ($St < 0.1$). Larger differences are observed at the highest frequencies ($St > 0.8$), but this range did not receive adequate forcing during the system identification experiment and therefore falls outside of the range of frequencies that was meant to be captured by the NLTF model. In addition, the observation that $St = 0.2$ to 0.6 is well-captured indicates that the model is capable of accounting for the emergence of the type-2 mode since this frequency range contains the transition from type 1 to type 2 and then back to type 1 (see Fig. 7). The instantaneous signals of u and \hat{u} at $x/D = 1$ in Fig. 14(b) also show good agreement. While there are some instances where \hat{u} shows larger differences from u (e.g., near $tU_\infty/D = 2$), the general behavior of the output signal is well-captured by the NLTF model at $x/D = 1$. There is also no clear phase shift between u and \hat{u} , indicating that the phase information is well-captured by the model. Instead, we can see that the discrepancies lie mainly in the amplitude of the estimated fluctuations. The PSD of u and \hat{u} at $x/D = 2$ in Fig. 14(c) reveals that the frequency content is not as well captured by the NLTF model when it is applied to the velocity fluctuations farther downstream. We see similar differences at the higher frequencies, but the discrepancy at

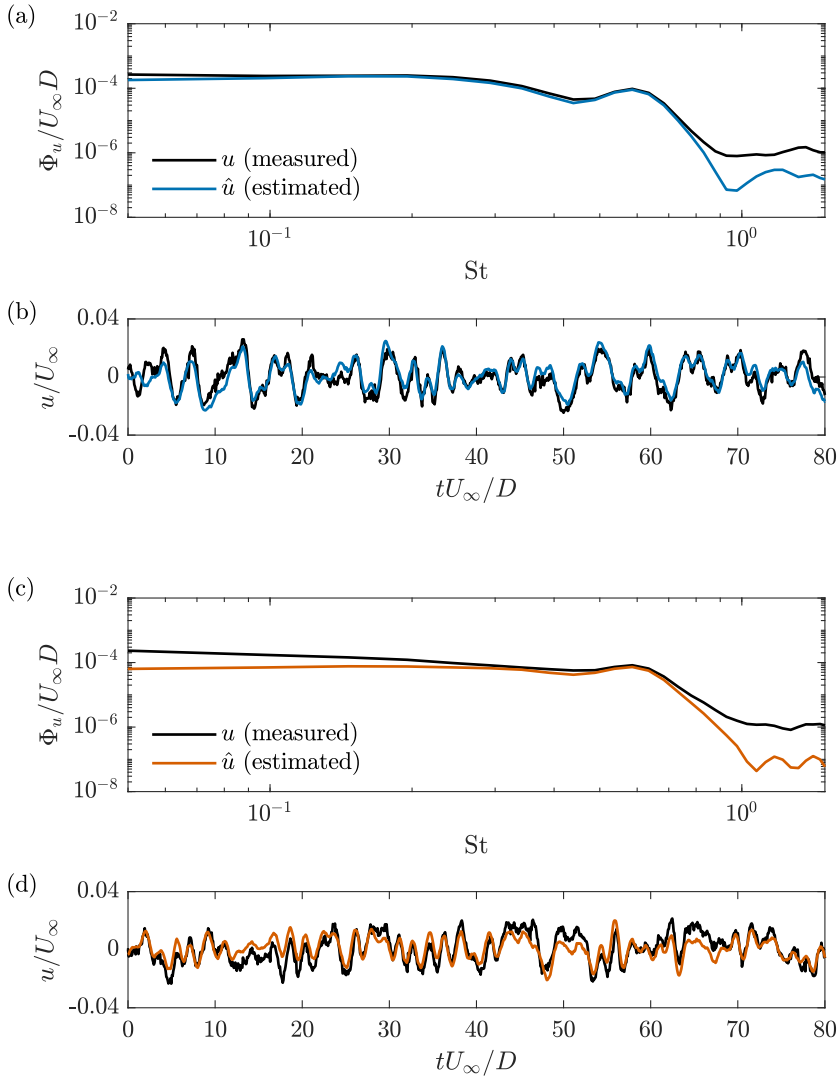


FIG. 14. The PSD and instantaneous samples of the streamwise velocity fluctuations that were measured (u) and estimated by the NLTF model (\hat{u}) at (a, b) $x/D = 1$ and (c, d) $x/D = 2$.

the lowest frequencies is much larger and now extends up to roughly $St = 0.3$. Despite this, the instantaneous signals of u and \hat{u} at $x/D = 2$ in Fig. 14(d) reveal that the behavior of the signal is still captured relatively well by the NLTF model, although it is clear that there are instances where the discrepancy between u and \hat{u} becomes somewhat large (e.g., near $tU_\infty/D = 65$). Once again, there is no clear phase shift between u and \hat{u} ; the discrepancies appear to be associated with the amplitudes.

Overall, the NLTF model does a reasonable job of capturing the input-output dynamics of the actuated flow. This type of model can be used to implement various control techniques, for example inverse feedforward control [74]. The associated impulse response can also be used with the eigensystem realization algorithm [76] to obtain a state-space model of the actuated flow, thus opening the door to many of the tools from modern control theory.

V. SUMMARY AND CONCLUSIONS

The present work considers the use of active wall-normal surface deformations as an actuation strategy for the control of wall-bounded flows. For this purpose, we have developed an electromagnetically driven “active surface” with diameter D . The investigation was conducted using a laminar boundary layer to provide insight into how surface deformations influence wall-bounded flows in general and to allow for the exploration of a linear modeling technique, the performance of which cannot be easily evaluated in a turbulent flow. We considered periodic and random operation of the active surface, with the latter being used for the purpose of system identification. The resulting motions were captured using high-speed PIV.

Operating the active surface to produce periodic (sinusoidal) surface deformations allowed for studying the resulting motions as a function of the frequency and amplitude of actuation. In general, periodic actuation produces modes featuring a repeating series of high- and low-speed motions with similar magnitudes. The high-speed motions form as the surface moves downwards and suction high-speed fluid toward the wall, while the low-speed motions form as the surface moves upwards and pushes low-speed fluid away from the wall. We found that the frequency of actuation determines the spatial structure of the resulting modes, while the amplitude of actuation determines their strength.

The spatial structures of the modes undergo two primary changes as the actuation frequency (f_a) is increased. First, the streamwise wavelength decreases proportionally to $St^{-0.7}$ where $St = f_a D / U_\infty$ is the Strouhal number. Second, the modes experience an alternating series of transitions between two distinct mode types. We define the type-1 modes as those featuring high- and low-speed motions with single maximums and minimums along $z = 0$. In contrast, the type-2 modes are those featuring high- and low-speed motions with double maxima and minima displaced in the spanwise directions. Type-1 modes were found for $St = 0.1, 0.2, 0.6,$ and 0.7 , while type-2 modes were found for the remaining St investigated here.

The spatial structure of the modes produced at a given frequency does not change much as the amplitude of the periodic deformation is increased. Interestingly, this is also true when considering the height of the resulting motions, which appears to remain similar despite the fourfold increase in the magnitude of the surface deformations considered here. Instead, increasing the amplitude increases the strength of the resulting velocity fluctuations, and this often leads to highly unstable motions that eventually break down. The present results indicate that small amplitudes and low frequencies generally produce modes that are more stable. Moreover, we found that the lowest frequencies of $St = 0.1$ and 0.2 produce the strongest type-1 velocity fluctuations. Considering the strength, stability, and type-1 structure of the motions produced at $St = 0.1$ and 0.2 , we can conclude that it is these low frequencies that offer the best performance for flow control purposes.

Finally, we employed a data-driven technique to identify a simple linear model for the input-output dynamics of the actuated flow. A nonparametric linear transfer function was obtained using a Wiener filter applied to a training data set with a randomized input. The characteristics of this transfer function agree well with the previous results obtained using periodic forcing. Comparison to the results from an evaluation data set indicates that the simple linear model is capable of capturing the input-output dynamics of the actuated flow, especially in the region immediately downstream from the active surface. This type of linear model provides access to many of the tools from modern control theory, and so this result is promising for the future use of active surface deformations as an actuation strategy for flow control applications.

ACKNOWLEDGMENTS

We acknowledge the support of the Natural Sciences and Engineering Research Council of Canada (NSERC) (Alexander Graham Bell Canada Graduate Scholarship–Doctoral; Discovery Grant No. RGPIN-2020-07231 Ghaemi, Smart skin for control of wall-bounded turbulent flows).

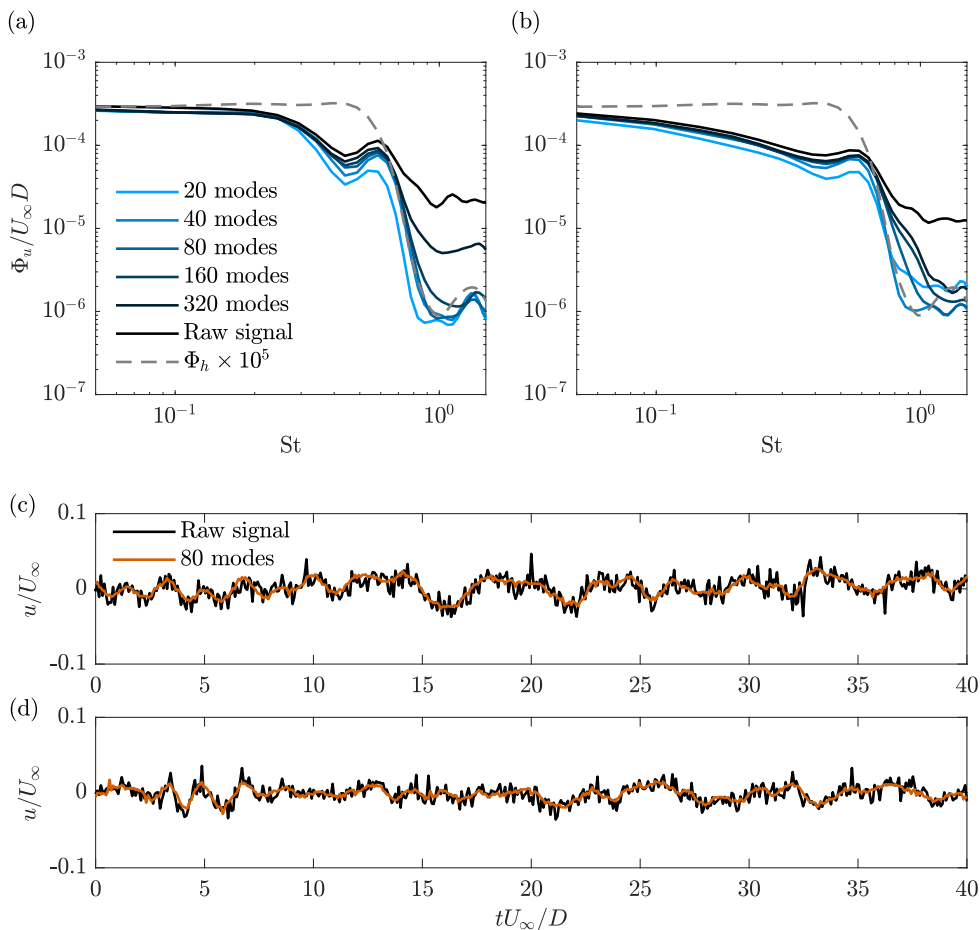


FIG. 15. PSD and instantaneous samples of the streamwise velocity fluctuations from the evaluation data set reconstructed using varying numbers of POD modes. The results are plotted for (a, c) $x/D = 1$, $y/D = 0.03$ and (b, d) $x/D = 2$, $y/D = 0.03$. The PSD of the forcing input (Φ_h) is shown (scaled) for reference.

APPENDIX: NOISE REDUCTION OF THE SYSTEM IDENTIFICATION DATA SETS

Here we describe how POD was used to reduce the PIV noise within the data sets used for system identification. We applied the method of snapshots [70] to an isolated region within FOV1 defined by $0.5 \leq x/D \leq 2.5$ and $0 \leq y/D \leq 0.2$. This region was isolated because it reduces the computations required for POD while retaining the entirety of the fluctuating velocity field downstream from the active surface. This data was then reconstructed using varying numbers of POD modes to identify the point at which the basis should be truncated to reduce the PIV noise. Figures 15(a) and 15(b) show the PSD of the fluctuating velocity signals extracted from the evaluation data set at $x/D = 1$ and 2 ($y/D = 0.03$) after being reconstructed using varying numbers of POD modes. The PSD of the random forcing input is also shown (scaled) for reference to highlight the frequency at which a large drop in the PSD of the velocity signal is expected. The frequencies up to this drop-off will be referred to as the relevant frequency range.

The PSD of the raw signals at both $x/D = 1$ and 2 show a large spectral density at frequencies beyond those of the forcing input. This noise floor is a result of the high-frequency PIV noise and is therefore not physical. Figures 15(a) and 15(b) reveal that the noise floor drops significantly when

fewer POD modes are used to reconstruct the data. However, if the number of modes used for reconstruction is too small, then the spectral density reduces substantially in the relevant frequency range as well, indicating that some physical variation within the data set is not being captured. We must therefore reconstruct the data using a number of POD modes that maximizes the reduction of the noise floor while minimizing the loss of spectral density in the relevant frequency range. This will result in a noise-reduced data set that still captures the physical variations within the velocity field.

By inspection of Figs. 15(a) and 15(b), we have elected to reconstruct the system identification data sets using the first 80 POD modes. As can be seen in the figure, this balances the two requirements of noise reduction in the high-frequency range and spectral density retention in the relevant frequency range. Instantaneous samples of the reconstructed streamwise velocity fluctuation compared to the raw signal at $x/D = 1$ and 2 are shown in Figs. 15(c) and 15(d). These results reveal that the reconstructed data do a good job of capturing the variation of the velocity field while greatly reducing the high-frequency PIV noise.

-
- [1] M. Gad-el-Hak, *Flow Control: Passive, Active, and Reactive Flow Management* (Cambridge University Press, Cambridge, UK, 2000).
 - [2] S. S. Collis, R. D. Joslin, A. Seifert, and V. Theofilis, Issues in active flow control: Theory, control, simulation, and experiment, *Prog. Aerosp. Sci.* **40**, 237 (2004).
 - [3] S. L. Brunton and B. R. Noack, Closed-loop turbulence control: Progress and challenges, *Appl. Mech. Rev.* **67**, 050801 (2015).
 - [4] L. N. Cattafesta and M. Sheplak, Actuators for active flow control, *Annu. Rev. Fluid Mech.* **43**, 247 (2011).
 - [5] E. J. Gutmark and F. F. Grinstein, Flow control with noncircular jets, *Annu. Rev. Fluid Mech.* **31**, 239 (1999).
 - [6] A. Glezer and M. Amitay, Synthetic jets, *Annu. Rev. Fluid Mech.* **34**, 503 (2002).
 - [7] S. Raghu, Fluidic oscillators for flow control, *Exp. Fluids* **54**, 1455 (2013).
 - [8] T. C. Corke, C. L. Enloe, and S. P. Wilkinson, Dielectric barrier discharge plasma actuators for flow control, *Annu. Rev. Fluid Mech.* **42**, 505 (2010).
 - [9] J.-J. Wang, K.-S. Choi, L.-H. Feng, T. N. Jukes, and R. D. Whalley, Recent developments in DBD plasma flow control, *Prog. Aerosp. Sci.* **62**, 52 (2013).
 - [10] J. Kriegseis, B. Simon, and S. Grundmann, Towards in-flight applications? A review on dielectric barrier discharge-based boundary-layer control, *Appl. Mech. Rev.* **68**, 020802 (2016).
 - [11] D. Munday and J. Jacob, Active control of separation on a wing with oscillating camber, *J. Aircraft* **39**, 187 (2002).
 - [12] W. W. Huebsch, Two-dimensional simulation of dynamic surface roughness for aerodynamic flow control, *J. Aircraft* **43**, 353 (2006).
 - [13] C. Thill, J. Etches, I. Bond, K. Potter, and P. Weaver, Morphing skins, *Aeronaut. J.* **112**, 117 (2008).
 - [14] W. W. Huebsch, P. D. Gall, S. D. Hamburg, and A. P. Rothmayer, Dynamic roughness as a means of leading-edge separation flow control, *J. Aircraft* **49**, 108 (2012).
 - [15] E. P. DeMauro, H. Dell’Orso, S. Zaremski, C. M. Leong, and M. Amitay, Control of laminar separation bubble on NACA 0009 airfoil using electroactive polymers, *AIAA J.* **53**, 2270 (2015).
 - [16] G. Jones, M. Santer, M. Debiassi, and G. Papadakis, Control of flow separation around an airfoil at low Reynolds numbers using periodic surface morphing, *J. Fluids Struct.* **76**, 536 (2018).
 - [17] M. G. C. Garland, M. S. Santer, and J. F. Morrison, Control of cellular separation using adaptive surfaces, *J. Fluids Struct.* **91**, 102609 (2019).
 - [18] Y. Mito and N. Kasagi, DNS study of turbulence modification with streamwise-uniform sinusoidal wall-oscillation, *Int. J. Heat Fluid Flow* **19**, 470 (1998).

- [19] M. Itoh, S. Tamano, K. Yokota, and S. Taniguchi, Drag reduction in a turbulent boundary layer on a flexible sheet undergoing a spanwise traveling wave motion, *J. Turbul.* **7**, N27 (2006).
- [20] S. Klumpp, M. Meinke, and W. Schröder, Drag reduction by spanwise transversal surface waves, *J. Turbul.* **11**, N22 (2010).
- [21] S. Klumpp, M. Meinke, and W. Schröder, Friction drag variation via spanwise transversal surface waves, *Flow Turbul. Combust.* **87**, 33 (2011).
- [22] S. Tamano and M. Itoh, Drag reduction in turbulent boundary layers by spanwise traveling waves with wall deformation, *J. Turbul.* **13**, N9 (2012).
- [23] S. R. Koh, P. Meysonnat, M. Meinke, and W. Schröder, Drag reduction via spanwise transversal surface waves at high Reynolds numbers, *Flow Turbul. Combust.* **95**, 169 (2015).
- [24] D. Roggenkamp, W. Jessen, W. Li, M. Klaas, and W. Schröder, Experimental investigation of turbulent boundary layers over transversal moving surfaces, *CEAS Aeronaut. J.* **6**, 471 (2015).
- [25] D. Roggenkamp, W. Li, M. Klaas, and W. Schröder, Influence of spanwise transversal surface wave on coherent structures in turbulent boundary layers, *Aerosp. Sci. Technol.* **86**, 387 (2019).
- [26] P. S. Meysonnat, D. Roggenkamp, W. Li, B. Roidl, and W. Schröder, Experimental and numerical investigation of transversal traveling surface waves for drag reduction, *Eur. J. Mech. B Fluids* **55**, 313 (2016).
- [27] M. Albers, P. S. Meysonnat, and W. Schröder, Actively reduced airfoil drag by transversal surface waves, *Flow Turbul. Combust.* **102**, 865 (2019).
- [28] M. Albers, P. S. Meysonnat, D. Fernex, R. Semaan, B. R. Noack, and W. Schröder, Drag reduction and energy saving by spanwise traveling transversal surface waves for flat plate flow, *Flow Turbul. Combust.* **105**, 125 (2020).
- [29] W. Li, D. Roggenkamp, V. Paakkari, M. Klaas, J. Soria, and W. Schröder, Analysis of a drag reduced flat plate turbulent boundary layer via uniform momentum zones, *Aerosp. Sci. Technol.* **96**, 105552 (2020).
- [30] S. A. Jacobson and W. C. Reynolds, Active control of streamwise vortices and streaks in boundary layers, *J. Fluid Mech.* **360**, 179 (1998).
- [31] W. -P. Jeon and R. F. Blackwelder, Perturbations in the wall region using flush mounted piezoceramic actuators, *Exp. Fluids* **28**, 485 (2000).
- [32] D.-H. Kim, J.-W. Chang, and J.-S. Cho, Flow disturbances depending on excitation frequency on a flat plate by a piezoceramic actuator, *J. Vis.* **16**, 111 (2013).
- [33] H. L. Bai, Y. Zhou, W. G. Zhang, S. J. Xu, Y. Wang, and R. A. Antonia, Active control of a turbulent boundary layer based on local surface perturbation, *J. Fluid Mech.* **750**, 316 (2014).
- [34] Z. X. Qiao, Y. Zhou, and Z. Wu, Turbulent boundary layer under the control of different schemes, *Proc. R. Soc. A* **473**, 20170038 (2017).
- [35] Z. X. Qiao, Z. Wu, and Y. Zhou, Turbulent boundary layer manipulation under a proportional-derivative closed-loop scheme, *Phys. Fluids* **30**, 115101 (2018).
- [36] Z. Tang, N. Jiang, X. Zheng, and Y. Wu, Local dynamic perturbation effects on amplitude modulation in turbulent boundary layer flow based on triple decomposition, *Phys. Fluids* **31**, 025120 (2019).
- [37] Z. Tang, X. Ma, N. Jiang, X. Cui, and X. Zheng, Local dynamic perturbation effects on the scale interactions in wall turbulence, *J. Turbul.* **22**, 208 (2021).
- [38] Z. Tang and N. Jiang, The effect of a synthetic input on small-scale intermittent bursting events in near-wall turbulence, *Phys. Fluids* **32**, 015110 (2020).
- [39] T. Segawa, Y. Kawaguchi, Y. Kikushima, and H. Yoshida, Active control of streak structures in wall turbulence using an actuator array producing inclined wavy disturbances, *J. Turbul.* **3**, N15 (2002).
- [40] I. Jacobi and B. J. McKeon, Dynamic roughness perturbations of a turbulent boundary layer, *J. Fluid Mech.* **688**, 258 (2011).
- [41] I. Jacobi and B. J. McKeon, Phase-relationships between scales in the perturbed turbulent boundary layer, *J. Turbul.* **18**, 1120 (2017).
- [42] S. Duvvuri and B. McKeon, Phase relations in a force turbulent boundary layer: Implications for modelling of high Reynolds number wall turbulence, *Philos. Trans. R. Soc. A* **375**, 20160080 (2017).
- [43] S. Gildersleeve, B. A. Tuna, and M. Amitay, Interactions of a low-aspect-ratio cantilevered dynamic pin with a boundary layer, *AIAA J.* **55**, 2142 (2017).

- [44] B. J. McKeon, I. Jacobi, and S. Duvvuri, Dynamic roughness for manipulation and control of turbulent boundary layers: An overview, *AIAA J.* **56**, 2178 (2018).
- [45] M. Amitay and S. Gildersleeve, Virtual and physical surface modifications as means of flow control, *AIAA J.* **57**, 53 (2019).
- [46] D. Huynh and B. McKeon, Characterization of the spatio-temporal response of a turbulent boundary layer to dynamic roughness, *Flow Turbul. Combust.* **104**, 293 (2020).
- [47] D. Huynh and B. McKeon, Measurements of a turbulent boundary layer-compliant surface system in response to targeted, dynamic roughness forcing, *Exp. Fluids* **61**, 94 (2020).
- [48] Z. Tang, Z. Fan, X. Ma, N. Jiang, B. Wang, Y. Huang, X. Qiu, Q. Zhou, Z. Lu, and Y. Liu, Tomographic particle image velocimetry flow structures downstream of a dynamic cylindrical element in a turbulent boundary layer by multi-scale proper orthogonal decomposition, *Phys. Fluids* **32**, 125109 (2020).
- [49] D. P. Huynh, Y. Huang, and B. J. McKeon, Experiments and modeling of a compliant wall response to a turbulent boundary layer with dynamic roughness forcing, *Fluids* **6**, 173 (2021).
- [50] K. S. Breuer, J. H. Haritonidis, and M. T. Landahl, The control of transient disturbances in a flat plate boundary layer through active wall motion, *Phys. Fluids A* **1**, 574 (1989).
- [51] L. M. Hofmann and T. Herbert, Disturbances produced by motion of an actuator, *Phys. Fluids* **9**, 3727 (1997).
- [52] C. Kim, W. -P. Jeon, J. Park, and H. Choi, Effect of a localized time-periodic wall motion on a turbulent boundary layer flow, *Phys. Fluids* **15**, 265 (2003).
- [53] S. Dearing, S. Lambert, and J. Morrison, Flow control with active dimples, *Aeronaut. J.* **111**, 705 (2007).
- [54] H. A. Carlson and J. L. Lumley, Active control in the turbulent wall layer of a minimal flow unit, *J. Fluid Mech.* **329**, 341 (1996).
- [55] T. Endo, N. Kasagi, and Y. Suzuki, Feedback control of wall turbulence with wall deformation, *Int. J. Heat Fluid Flow* **21**, 568 (2000).
- [56] S. Kang and S. Choi, Active wall motions for skin-friction drag reduction, *Phys. Fluids* **12**, 3301 (2000).
- [57] M. Pamiès, E. Garnier, A. Merlen, and P. Sagaut, Opposition control with arrayed actuators in the near-wall region of a spatially developing turbulent boundary layer, *Int. J. Heat Fluid Flow* **32**, 621 (2011).
- [58] W. -Y. Zhang, W. -X. Huang, C. -X. Xu, and G. -X. Cui, Suboptimal control of wall turbulence with arrayed dimple actuators for drag reduction, *J. Turbul.* **17**, 379 (2016).
- [59] M. -W. Ge, L. Fang, and Y. -Q. Liu, Drag reduction of wall bounded incompressible turbulent flow based on active dimples/pimples, *J. Hydrodyn.* **29**, 261 (2017).
- [60] N. Goldin, R. King, A. Pätzold, W. Nitsche, D. Haller, and P. Woias, Laminar flow control with distributed surface actuation: damping Tollmien-Schlichting waves with active surface displacement, *Exp. Fluids* **54**, 1478 (2013).
- [61] R. E. Hanson, H. P. Buckley, and P. Lavoie, Aerodynamic optimization of the flat-plate leading edge for experimental studies of laminar and transitional boundary layers, *Exp. Fluids* **53**, 863 (2012).
- [62] B. Gibeau and S. Ghaemi, The mode B structure of streamwise vortices in the wake of a two-dimensional blunt trailing edge, *J. Fluid Mech.* **884**, A12 (2020).
- [63] M. R. Johnson and L. W. Kostiuik, Efficiencies of low-momentum jet diffusion flames in crosswinds, *Combust. Flame* **123**, 189 (2000).
- [64] B. Gibeau, D. Gingras, and S. Ghaemi, Evaluation of a full-scale helium-filled soap bubble generator, *Exp. Fluids* **61**, 28 (2020).
- [65] J. Westerweel and F. Scarano, Universal outlier detection for PIV data, *Exp. Fluids* **39**, 1096 (2005).
- [66] B. Wieneke, Stereo-PIV using self-calibration on particle images, *Exp. Fluids* **39**, 267 (2005).
- [67] H. Schlichting and K. Gersten, *Boundary-Layer Theory* (Springer, Berlin, 2017).
- [68] S. A. Maslowe, Critical layers in shear flows, *Annu. Rev. Fluid Mech.* **18**, 405 (1986).
- [69] See Supplemental Material at <http://link.aps.org/supplemental/10.1103/PhysRevFluids.7.114101> for high-speed videos of the active surface operating at the maximum amplitude of 2 mm and actuation frequencies of 20 and 40 Hz.
- [70] L. Sirovich, Turbulence and the dynamics of coherent structures, Parts I–III, *Q. Appl. Math.* **45**, 561 (1987).

- [71] P. J. Schmid and D. S. Henningson, *Stability and Transition in Shear Flows* (Springer-Verlag, New York, NY, 2001).
- [72] R. Rathnasingham and K. S. Breuer, Active control of turbulent boundary layers, *J. Fluid Mech.* **495**, 209 (2003).
- [73] F. Juillet, B. J. McKeon, and P. J. Schmid, Experimental control of natural perturbations in channel flow, *J. Fluid Mech.* **752**, 296 (2014).
- [74] P. P. C. Brito, P. Morra, A. V. G. Cavalieri, T. B. Araújo, D. S. Henningson, and A. Hanifi, Experimental control of Tollmien-Schlichting waves using pressure sensors and plasma actuators, *Exp. Fluids* **62**, 32 (2021).
- [75] M. H. Hayes, *Statistical Digital Signal Processing and Modeling* (John Wiley & Sons, New York, NY, 1996).
- [76] S. L. Brunton and J. N. Kutz, *Data Driven Science and Engineering: Machine Learning, Dynamical Systems, and Control* (Cambridge University Press, Cambridge, UK, 2019).